

# Comparison of numerical models for computing underwater light fields

Curtis D. Mobley, Bernard Gentili, Howard R. Gordon, Zhonghai Jin, George W. Kattawar, André Morel, Phillip Reinersman, Knut Stamnes, and Robert H. Stavn

Seven models for computing underwater radiances and irradiances by numerical solution of the radiative transfer equation are compared. The models are applied to the solution of several problems drawn from optical oceanography. The problems include highly absorbing and highly scattering waters, scattering by molecules and by particulates, stratified water, atmospheric effects, surface-wave effects, bottom effects, and Raman scattering. The models provide consistent output, with errors (resulting from Monte Carlo statistical fluctuations) in computed irradiances that are seldom larger, and are usually smaller, than the experimental errors made in measuring irradiances when using current oceanographic instrumentation. Computed radiances display somewhat larger errors.

## 1. Introduction

Various numerical models are now in use for computing underwater irradiances and radiance distributions. These models were designed to address a wide range of oceanographic problems. The models are based on various simplifying assumptions, have differing levels of sophistication in their representation of physical processes, and use several different numerical solution techniques.

In spite of the increasingly important roles these numerical models are playing in optical oceanography, the models remain incompletely validated in the sense that their outputs have not been extensively compared with measured values of the quantities they predict. This desirable model-data comparison

is not presently possible because the requisite comprehensive oceanic optical data sets are not available. Such data sets must contain simultaneous measurements of the inherent optical properties of the sea water (e.g., the absorption and scattering coefficients and the scattering phase function), environmental parameters (e.g., the sky radiance distribution and sea state), and radiometric quantities (e.g., the complete radiance distribution or various irradiances). The inherent optical properties and the environmental parameters are needed as input to the numerical models; the radiometric variables are the quantities predicted by the models. Current developments in oceanic optical instrumentation and measurement methodologies give cause for hope that data sets that are adequate for comprehensive model-data comparisons will become available within the next few years.

Meanwhile, our faith in these models' predictions rests on careful debugging of computer codes, internal checks such as conservation of energy or known relations between inherent and apparent optical properties, simulation of a few grossly simplified situations for which analytical solutions of the radiative transfer equation are available, and comparison (sometimes indirect) with incomplete data sets. An additional worthwhile check on the various models can be made by applying them to a common set of realistic problems. Such model-model comparisons help to identify errors in coding or weaknesses in the mathematical representation of physical phenomena, quantify numerical errors particular to the various solution algorithms, determine optimum numerical techniques for simulation of particular physical phe-

---

C. D. Mobley is with the Jet Propulsion Laboratory, California Institute of Technology, Mail Stop 300-323, 4800 Oak Grove Drive, Pasadena, California 91109; B. Gentili and A. Morel are with the Laboratoire de Physique et Chimie Marines, Université Pierre et Marie Curie, F06230 Villefranche-sur-Mer, France; H. R. Gordon is with the Department of Physics, University of Miami, Coral Gables, Florida 33124; Z. Jin and K. Stamnes are with the Geophysical Institute, University of Alaska, Fairbanks, Alaska 99701; G. W. Kattawar is with the Department of Physics, Texas A & M University, College Station, Texas 77843; P. Reinersman is with the Department of Marine Science, University of South Florida, St. Petersburg, Florida 33701; and R. H. Stavn is with the Department of Biology, University of North Carolina, Greensboro, North Carolina 27412.

Received 19 January 1993.

0003-6935/93/367484-21\$06.00/0.

© 1993 Optical Society of America.

nomena, and determine which models might be appropriate for inclusion in a future library of underwater radiative transfer codes corresponding to those now available for atmospheric radiative transfer modeling (such as LOWTRAN<sup>1</sup>).

In March 1991 the Oceanic Optics Program of the Office of Naval Research sponsored a workshop to foster a close examination of the various models now in use and to begin the process of model-model comparison. This paper reports the results of that comparison. The models being evaluated are described in Section 2. During the workshop the participants defined a set of canonical (standard) problems for use in model comparisons. These problems are documented in Section 3. Section 4 presents selected results obtained when the models of Section 2 are applied to the problems of Section 3.

## 2. Numerical Models

All the numerical models compared here generate an approximate solution to the time-independent, monochromatic radiative transfer equation in one spatial dimension:

$$\mu \frac{\partial L(\tau; \mu, \phi)}{\partial \tau} = -L(\tau; \mu, \phi) + \omega_0(\tau) \iint_{(\mu', \phi') \in \Xi} L(\tau; \mu', \phi') \times \tilde{\beta}(\tau; \mu', \phi' \rightarrow \mu, \phi) d\mu' d\phi' + S(\tau; \mu, \phi). \quad (1)$$

Here  $L(\tau; \mu, \phi)$  is the unpolarized spectral radiance (at wavelength  $\lambda$ , omitted for brevity) at optical depth  $\tau$  and in direction  $(\mu, \phi)$ ,  $\omega_0$  is the scattering-to-attenuation ratio,  $\beta$  is the scattering phase function, and  $S$  represents any internal source of radiance. The depth  $\tau$  is measured positive downward from the mean sea surface, and the polar angle  $\theta = \cos^{-1} \mu$  is measured from the nadir direction. (See Table 1 for a list of symbols and their units and definitions.) To solve Eq. (1) within a water body, it is necessary to specify (a) the inherent optical properties of the water body,  $\omega_0$  and  $\beta$ ; (b) the distribution of internal sources  $S$ ; (c) the radiance distribution that is externally incident upon the boundaries of the water body; and (d) the physical nature of the boundaries themselves.

The models differ primarily in the mathematical techniques used to solve Eq. (1) and in the treatment of boundary conditions at the sea surface. Two of the models described below (models II and DO) use analytical (invariant imbedding and discrete ordinates) techniques for solving Eq. (1), and five of the models (MC1-MC5) use probabilistic (Monte Carlo) techniques. Each of the models, as applied to the solution of the canonical problems defined in Section 3, solves Eq. (1) for a plane-parallel water body that is laterally homogeneous but may be inhomogeneous with depth. The upper boundary of the water body is the windblown, random air-water interface. The lower boundary is either an infinitely thick layer of water below the greatest depth of interest or an

Table 1. Significant Symbols, Units, and Definitions

Symbol	Units	Definition
$\lambda$	nm	Wavelength of light
$\psi$	deg	Scattering angle; $0 \leq \psi \leq 180^\circ$
$\theta$	deg	Polar angle of photon travel, measured from the nadir, $0 \leq \theta \leq 180^\circ$
$\phi$	deg	Azimuthal angle of photon travel, measured counterclockwise (looking downward) from the downwind direction, $0 \leq \phi < 360^\circ$
$\mu$	—	$\mu \equiv \cos \theta$ ; alternate way to specify the polar angle, $-1 \leq \mu \leq 1$
$\theta_v$	deg	Polar viewing angle; $\theta_v = 180^\circ - \theta$
$\phi_v$	deg	Azimuthal viewing angle; $\phi_v = 180^\circ + \phi$
$\Omega$	sr	Solid angle; a differential element is $d\Omega = \sin \theta d\theta d\phi = d\mu d\phi$
$\Xi_d$	—	Set of all downward directions; $\int_{\Xi_d} d\Omega = 2\pi$ sr
$\Xi_u$	—	Set of all upward directions; $\int_{\Xi_u} d\Omega = 2\pi$ sr
$z$	m	Geometric depth, measured positive downward
$\tau$	—	Optical depth, measured positive downward: $\tau \equiv \int_0^z c(z) dz$
$\sigma$	—	Standard deviation of the surface-wave slope
$a_w$	$m^{-1}$	Absorption coefficient for pure sea water
$a_p$	$m^{-1}$	Absorption coefficient for suspended particles
$a$	$m^{-1}$	Total absorption coefficient: $a \equiv a_w + a_p$
$b_w$	$m^{-1}$	Scattering coefficient for pure sea water
$b_p$	$m^{-1}$	Scattering coefficient for suspended particles
$b$	$m^{-1}$	Total scattering coefficient: $b \equiv b_w + b_p$
$c$	$m^{-1}$	Total attenuation coefficient: $c \equiv a + b$
$\beta$	$m^{-1} \text{ sr}^{-1}$	Volume scattering function
$\tilde{\beta}$	$\text{sr}^{-1}$	Scattering phase function, $\tilde{\beta} \equiv \beta/b$
$\omega_0$	—	Scattering-to-attenuation ratio, $\omega_0 \equiv b/c$
$L$	$\text{W m}^{-2} \text{ sr}^{-1}$	Radiance distribution, $L = L(z, \theta, \phi)$ or $L(\tau, \mu, \phi)$
$L_u$	$\text{W m}^{-2} \text{ sr}^{-1}$	Nadir radiance, $L_u \equiv L_u(\tau) \equiv L(\tau, \theta = 180^\circ, \phi = 0)$
$L_\infty$	$\text{W m}^{-2} \text{ sr}^{-1}$	Asymptotic radiance distribution
$k_\infty$	—	Asymptotic diffuse attenuation coefficient
$S$	$\text{W m}^{-2} \text{ sr}^{-1}$	Internal source of radiance
$E_\perp$	$\text{W m}^{-2} \text{ nm}^{-1}$	Irradiance on a surface perpendicular to the sun's rays
$E_d$	$\text{W m}^{-2} \text{ nm}^{-1}$	Downwelling plane irradiance: $E_d(\tau) \equiv \int_{\Xi_d} L(\tau, \mu, \phi)  \mu  d\Omega$
$E_u$	$\text{W m}^{-2} \text{ nm}^{-1}$	Upwelling plane irradiance: $E_u(\tau) \equiv \int_{\Xi_u} L(\tau, \mu, \phi)  \mu  d\Omega$
$E_{ou}$	$\text{W m}^{-2} \text{ nm}^{-1}$	Upwelling scalar irradiance: $E_{ou}(\tau) \equiv \int_{\Xi_u} L(\tau, \mu, \phi) d\Omega$

opaque, reflecting bottom at a finite depth. The models all assume that externally applied radiance is incident downward upon the upper side of the air-water surface. The models are all monochromatic, and there are no internal sources of radiance (such as bioluminescence). However, some of the models can simulate inelastic-scattering processes by sequential solutions of Eq. (1). For example, the model is first

run at the wavelength of excitation,  $\lambda_{\text{ex}}$ , to compute the energy shifted by inelastic scattering from  $\lambda_{\text{ex}}$  to another wavelength  $\lambda$ , and then the model is run again at  $\lambda$ , with the radiance shifted from  $\lambda_{\text{ex}}$  appearing as a source term  $S$  at  $\lambda$ . A particular example of  $S$  used in this treatment of Raman scattering is given in Appendix A. The models all account for multiple scattering and can use realistic scattering phase functions that are highly peaked in forward directions, as is the case for sea water.

Several of the models have additional capabilities, such as the computation of polarized radiance in the Stokes vector format and the simulation of azimuthally anisotropic random air-water surfaces. These capabilities are not evaluated in this paper.

All but one of the models directionally discretizes Eq. (1) by partitioning the set of all directions,  $\Xi$ , into a grid of quadrilateral regions bounded by lines of constant  $\mu$  and constant  $\phi$ , plus two polar caps (collectively called quads). The fundamental quantity computed by these models is the quad-averaged radiance defined by

$$L(\tau; u, v) \equiv \frac{1}{\Omega_{uv}} \iint_{(\mu, \phi) \in Q_{uv}} L(\tau; \mu, \phi) d\mu d\phi. \quad (2)$$

$L(\tau; u, v)$  is physically interpreted as the average radiance over the set of directions  $(\mu, \phi)$  contained in the  $uv$ th quad,  $Q_{uv}$  ( $u$  labels  $\mu$  bands and  $v$  labels  $\phi$  bands), which subtends a solid angle of size  $\Omega_{uv}$ . In the model comparison we chose to use 24  $\phi$  bands of uniform width  $\Delta\phi = 15^\circ$  and 20  $\mu$  bands of size  $\Delta\mu = 0.1$ . However, a polar cap with  $\Delta\mu = 0.1$  has a half-angle of  $\theta = 25.8^\circ$ , which is much larger than one would normally use in computing the nadir or zenith radiances. Therefore some models were run with a slightly different  $\mu$  spacing and smaller polar caps. The remaining model (DO) computes the radiance  $L(\tau; \mu, \phi)$  in particular  $(\mu, \phi)$  directions.

We now briefly describe the distinguishing features of the various models.

#### A. Model II [Invariant Imbedding, (Mobley)]

The integral operator of Eq. (2), which averages any quantity over the set of directions  $(\mu, \phi) \in Q_{uv}$ , can be applied to Eq. (1). The result is a quad-averaged radiative transfer equation in which  $L(\tau; \mu, \phi)$  is replaced by  $L(\tau; u, v)$ , integration over all directions is replaced by summation over all quads, and the phase function  $\beta(\tau; \mu', \phi' \rightarrow \mu, \phi)$  is replaced by a quad-averaged quantity  $\beta(\tau; r, s \rightarrow u, v)$  that specifies how much of the radiance initially headed into quad  $Q_{rs}$  gets scattered into quad  $Q_{uv}$ . By standard techniques of Fourier analysis and invariant imbedding theory, the equations for the  $L(\tau; u, v)$  are transformed into a set of Riccati differential equations governing the depth dependence of certain reflectance and transmittance functions within the water body. Depth integration of the Riccati equations (by a high-order Runge-Kutta algorithm) and incorporation of the boundary conditions at the sea surface and

bottom lead eventually to the desired  $L(\tau; u, v)$  at all depths. These mathematical operations are outlined in Mobley<sup>2</sup> and are described in full by Mobley and Preisendorfer.<sup>3</sup> The inherent optical properties of the water body can vary arbitrarily with depth. Absorption and scattering are built up as sums of terms representing the contributions by pure water, particles of various types, and dissolved substances.

This model uses a Monte Carlo simulation of the windblown sea surface to evaluate certain quad-averaged, bidirectional reflectance and transmittance functions that describe how the sea surface reflects and transmits radiance that is incident upon the surface from above and below. In this simulation, the sea surface is resolved into a grid of triangular wave facets with vertex elevations that are randomly determined from any chosen wave slope-wind speed spectrum in a manner described by Mobley and Preisendorfer<sup>3</sup> and by Preisendorfer and Mobley.<sup>4</sup> The surface simulation allows for multiple reflections of rays by wave facets and for the possibility of shadowing of one facet by another. The probabilistic ray-tracing calculations for setting up the surface boundary conditions are independent of the analytical computations within the water body. Moreover, because the ray tracing involves only the surface-wave facets, for which it is assumed that there is no absorption, no rays are lost to absorption. It is therefore computationally feasible to trace a sufficient number of rays to reduce the Monte Carlo fluctuations in the computed bidirectional surface functions to a negligible level.

This model does not include an atmosphere per se. The sky radiance that is incident upon the sea surface is obtained either from an analytic model (e.g., a cardioid distribution or the empirical model of Harrison and Coombes<sup>5</sup>) or from the output of a separately run atmospheric radiative transfer model. In the simulation of problem 4, below, LOWTRAN-7 was run to generate the sky radiance at the center of each of the  $\mu$ - $\phi$  quads; that value was then taken as the average sky radiance over the quad.

The bottom boundary can be either an infinitely thick homogeneous layer of water below some depth  $\tau_{\text{max}}$  or an opaque bottom at  $\tau_{\text{max}}$ . In the infinite-depth case, the bidirectional radiance reflectance properties of the infinite layer below  $\tau_{\text{max}}$  are obtained from an eigenmatrix analysis described by Preisendorfer.<sup>6</sup> The same analysis yields the asymptotic diffuse attenuation coefficient,  $k_\infty$ , and the asymptotic radiance distribution,  $L_\infty(\mu)$ , that are appropriate for the homogeneous layer. In the opaque-bottom case, the reflectance properties of the bottom are explicitly specified, for example, as a Lambertian surface with a given irradiance reflectance.

The chief advantage of this model is computational efficiency. Solution of the Riccati differential equations for  $L$  is an analytic process, and thus there are no Monte Carlo fluctuations in the computed radiances (except for a negligible amount introduced by the simulation of the sea surface). In particular,

both upwelling and downwelling radiances are computed with the same accuracy. Moreover, computation time is a linear function of depth, so that accurate radiance distributions are easily obtained at great depths ( $\tau > 10$ ). Computation time depends only mildly on quantities such as the scattering-to-attenuation ratio, surface boundary conditions, and water stratification. The associated computer code is available and is documented by Mobley.<sup>7</sup>

#### B. Model DO [Discrete Ordinates (Jin and Stamnes)]

This model solves Eq. (1) directly without applying the quad-averaging defined by Eq. (2). The radiance is expanded into a Fourier cosine series,  $L(\tau, \mu, \phi) = \sum_{m=0}^{2N-1} L^m(\tau, \mu) \cos(\phi - \phi_0)$ , and the phase function is expanded into a series of  $2N$  Legendre polynomials,

$$\begin{aligned} \tilde{\beta}(\tau; \mu', \phi' \rightarrow \mu, \phi) &\equiv \tilde{\beta}(\tau; \cos \psi) \\ &= \sum_{l=0}^{2N-1} (2l+1) g_l(\tau) P_l(\cos \psi), \end{aligned}$$

where  $g_l(\tau)$  is the expansion coefficient and  $\psi$  is the scattering angle. The advantage of these expansions is that the azimuthal dependence is isolated, in the sense that  $2N$  independent equations for the Fourier coefficients  $L^m(\tau, \mu)$  are obtained:

$$\begin{aligned} \mu \frac{dL^m(\tau, \mu)}{d\tau} &= -L^m(\tau, \mu) + \omega_0(\tau) \int_{-1}^1 L^m(\tau, \mu') \\ &\quad \times \beta^m(\tau; \mu', \mu) d\mu' + S^m(\tau, \mu), \end{aligned}$$

where

$$\begin{aligned} \beta^m(\tau; \mu', \mu) &= \frac{1}{2} \sum_{l=m}^{2N-1} (2l+1) g_l(\tau) \\ &\quad \times \frac{(l-m)!}{(l+m)!} P_l^m(\mu) P_l^m(\mu'). \end{aligned}$$

Here  $P_l^m(\mu)$  is the associated Legendre polynomial.

The atmosphere and the ocean are divided into a suitable number of layers to adequately resolve the optical properties of each of the two media. Each layer is taken to be homogeneous, but the optical properties are allowed to vary from layer to layer. For a homogeneous medium, only one layer is required. At the interface between the ocean and the atmosphere (assumed to be flat), Fresnel's formula is used to compute the appropriate reflection and transmission coefficients, and Snell's law is applied to account for the refraction taking place there.

The integral term in each of these azimuth-independent equations is then approximated by a Gaussian quadrature sum with  $2N_1$  terms (streams) in the atmosphere and  $2N_2$  terms in the ocean, so that there are  $2N_1$  streams in the refractive region of ocean that communicate directly with the atmosphere and  $2N_2 - 2N_1$  streams in the total reflection region of the ocean. In this way the integro-differential equation is transformed into a system of

coupled ordinary differential equations that is solved by the discrete ordinate method, as described in more detail elsewhere,<sup>8</sup> subject to appropriate boundary conditions at the top of the atmosphere and the bottom of the ocean. The basic discrete-ordinate method used here is described and thoroughly documented in previous publications.<sup>9-11</sup> The modifications required to apply the method to a system consisting of two adjacent media with different indices of refraction are described by Jin and Stamnes.<sup>8</sup>

This method has the following unique features: (i) Because the solution is analytic, the computational speed is completely independent of individual layer and total optical thickness, which may be taken to be arbitrarily large. The computational speed is directly proportional to the number of horizontal layers used to resolve the optical properties in the atmosphere and ocean. (ii) Accurate irradiances are obtained with just a few streams, which makes the code very efficient. (iii) Because the solution is analytic, radiances and irradiances can be returned at arbitrary optical depths unrelated to the computational levels. (iv) The DO method is essentially a matrix eigenvalue-eigenvector solution, from which the asymptotic solution is automatically obtained. The smallest eigenvalue is  $k_\infty$ , and the associated eigenvector is  $L_\infty$ .

Desirable and possible extensions of the method include (i) the computation of inelastic-scattering effects to treat phenomena such as Raman scattering and (ii) the inclusion of a windblown surface to simulate the basic features of sea-surface roughness. These extensions would require some modifications of the existing computer code.

#### C. Model MCI [Monte Carlo (Gordon)]

This model simulates radiative transfer in both the ocean and the atmosphere, as coupled across a wind-roughened interface. The code is designed to simulate irradiances as a function of depth for computation of the irradiance reflectance,  $E_u/E_d$ , and diffuse attenuation functions such as  $K_d = -d(\ln E_d)/dz$ . The nadir-viewing radiance,  $L_u$ , is also computed as a function of depth for the computation of  $Q = E_u/L_u$ . The optical properties of the ocean are continuously stratified in the vertical. They can be specified as discrete values as a function of depth (with linear interpolation between the given depths) or determined from formulas as in problem 3, below. Separate scattering phase functions are used for the particles and for the water itself. Variants of this code have been used for a number of studies of radiative transfer in the ocean.<sup>12-17</sup>

The sea-surface roughness is modeled using the Cox and Munk<sup>18</sup> surface slope distribution for a given wind speed. The effect of the surface roughness is not simulated exactly because the possibility of shadowing of one facet by another is ignored. Multiple scattering, however, is included: e.g., if a downward-moving photon in the atmosphere encounters the sea surface and is still moving downward after reflection,

it will undergo a second interaction with the sea surface. One important aspect of this model is the proper use of photon weights to account for the fact that not all facets are oriented in such a manner as to be able to interact with an incident photon, i.e., facets with normals making an angle less than  $90^\circ$  to the direction of the incident photon. The sequence of events during an interaction with the surface follows. From Cox and Munk, the probability that the  $x$  and  $y$  components of the surface slope,  $z_x$  and  $z_y$ , respectively, are within  $z_x \pm \frac{1}{2}dz_x$  and  $z_y \pm \frac{1}{2}dz_y$  is

$$p(z_x, z_y)dz_xdz_y = \frac{1}{\pi\sigma^2} \exp\left(-\frac{z_x^2 + z_y^2}{\sigma^2}\right)dz_xdz_y,$$

or

$$p(\theta_n, \phi_n)d\theta_nd\phi_n = \frac{1}{\pi\sigma^2} \exp\left(-\frac{\tan^2 \phi_n}{\sigma^2}\right) \times \tan \phi_n \sec^2 \phi_n d\theta_nd\phi_n.$$

where

$$\sigma^2 = 0.003 + 0.00512U.$$

Here  $U$  is the wind speed in meters per second,  $\phi_n$  is the angle between the normal to the facet and the normal to the level surface, and  $\theta_n$  is the azimuth of the normal. Given random numbers  $\rho_{\theta_n}$  and  $\rho_{\phi_n}$  on the unit interval  $(0, 1)$ , the model finds  $\theta_n$  and  $\phi_n$  from

$$\theta_n = 2\pi\rho_{\theta_n},$$

$$\rho_{\phi_n} = \frac{1}{2\pi^2\sigma^2} \int_0^{\phi_n} \exp\left(-\frac{\tan^2 \phi_n'}{\sigma^2}\right) \tan \phi_n' \sec^2 \phi_n' d\phi_n'.$$

The photon interacting with the surface is given the weight

$$W = \frac{\cos \omega \sec \phi_n}{\iint_{\cos \omega > 0} p(z_x, z_y) \cos \omega \sec \phi_n dz_x dz_y},$$

where  $\omega$  is the angle of incidence upon the chosen facet. The weight,  $W$ , accounts for sampling from  $p(z_x, z_y)$  even though all facets are not visible to the photon.

The atmospheric part of the model consists of fifty 1-km layers with both molecular and aerosol scattering. The vertical distribution of the optical properties is taken from Elterman.<sup>19</sup> The aerosol phase function at the given wavelength is determined from Mie theory<sup>20</sup> with Deirmendjian's Haze  $C$  size distribution<sup>21</sup>

$$\frac{dn(r)}{dr} \propto \frac{1}{r^{\nu+1}},$$

where  $r$  is the particle radius and  $dn(r)$  is the number of particles per unit volume with radius between  $r$

and  $r + dr$ ;  $\nu = 3$  is used in the computations. The aerosol total-scattering coefficient at each altitude is proportional to  $\lambda^{-P}$ , where  $P = \nu - 2$ ; however,  $P \approx 0.75$  fits Elterman's data better. When a photon interacts with the atmosphere, the scattering angle is chosen from either the molecular or aerosol phase functions based on the ratio of their scattering coefficients for the layer in which the interaction takes place.

When inelastic processes are to be included, the above code is operated at the excitation wavelength,  $\lambda_{\text{ex}}$ , to determine the excitation radiance distribution. This is used as input to a second Monte Carlo code that computes the light field at the wavelength of interest.<sup>17</sup> As with the elastically scattered radiation, the goal is to determine the irradiances of the inelastically scattered radiation. This is a considerable simplification because the solution can be effected by working with the azimuthally averaged radiance at  $\lambda$ ; i.e., only the azimuthally averaged radiative transfer equation need be solved. The details of this formulation are given in Appendix A.

#### D. Model MC2 (Monte Carlo 2, Kattawar)

This model also simulates a coupled ocean-atmosphere system. The Monte Carlo code relies heavily on several variance-reducing schemes to increase computational efficiency. We give only a brief description of one of the most useful ones. The use of statistical weights allows us to treat each photon history as a packet of photons rather than as a single photon. Photons are never allowed to escape from the ocean-atmosphere system. The method of forced collisions is used, whereby we sample from a biased distribution that ensures a collision along the path, and the weight is then adjusted appropriately to unbiased the result. The way this is done is as follows. Suppose one wants to compute the expectation value  $\langle f \rangle$  of some function  $f$  of a random variable  $x$ , using a probability density function  $p(x)$ . By definition,

$$\langle f \rangle = \int f(x)p(x)dx.$$

However, if we want to sample from the density function,  $\tilde{p}(x)$ , then

$$\langle f \rangle = \int f(x) \frac{p(x)}{\tilde{p}(x)} \tilde{p}(x) dx = \int f(x)w(x)\tilde{p}(x)dx,$$

where  $w(x) \equiv p(x)/\tilde{p}(x)$  is called the statistical weight. The variance  $\sigma^2$  of  $f(x)w(x)$  when sampling from the biased distribution is given by

$$\sigma^2[f(x)w(x)] = \int [f(x)w(x) - \langle f \rangle]^2 \tilde{p}(x) dx.$$

Although this method appears straightforward, it does have pitfalls. If the weight can have values that exceed unity, then one can have a variance that far exceeds the variance in the unbiased sampling.

Therefore extreme caution must be used when applying this method. It should be noted that this is a very powerful method for studying perturbation effects, because several processes can be simultaneously emulated with the same set of photon histories.

Now consider the technique of forced collisions, in which photons are never allowed to escape the medium. Let  $\tau_b$  denote the optical path length to a boundary. To ensure that the photon never escapes, we sample the path length according to the probability density function

$$\bar{p}(\tau)d\tau = \frac{\exp(-\tau)d\tau}{1 - \exp(-\tau_b)}, \quad 0 \leq \tau \leq \tau_b.$$

The weight now has to be multiplied by  $[1 - \exp(-\tau_b)]$  to remove the bias. It should be noticed that this factor is always less than unity and should produce a smaller variance than that produced when using unforced sampling. Histories are terminated only when the statistical weight falls below some specified value.

When an interaction occurs, the packet weight is multiplied by the single-scattering albedo,  $\omega_0$ , which gives the fraction of photons that can continue to scatter. The level air-water interface is modeled by using the appropriate Fresnel reflection and transmission coefficients. A random number is chosen at this stage to determine whether the photon is transmitted or reflected.

Radiances are obtained over detectors that have finite solid angles. However, statistical estimation can be used to give true continuum radiance values where no directional averaging is done. This model can simulate inelastic scattering; the details are given in Kattawar and Xu.<sup>22</sup> The Monte Carlo method has also been extended to include the full Stokes vector treatment of polarization;<sup>23-26</sup> these papers show that substantial errors can occur if polarization is neglected.

#### E. Model MC3 [Monte Carlo 3 (Morel and Gentili)]

This Monte Carlo model is similar to those described by Plass and Kattawar<sup>27,28</sup> and by Gordon and Brown.<sup>29</sup> It is designed to simulate the radiance distribution at any level in the atmosphere and in the ocean. Between these two media, a wind-roughened interface is modeled with the isotropic Gaussian distribution of sea-surface slopes, as discussed under model MC1. The probability of occurrence of the various slopes is modified when considering nonvertically incident photons. This photon-facet interaction is modeled as in Plass *et al.*,<sup>30</sup> it does not account for the possible occultation of a facet by an adjacent one. Transmitted and reflected photon packets resulting from interaction with the air-water surface are weighted according to Fresnel's law (including the possibility of total internal reflection). According to the problem under investigation, photon packets are introduced at the top of the atmosphere, or just above (or below) the ocean surface. For specific problems

involving deep levels, packets can be reintroduced at intermediate depths inside the water body, according to a directional distribution that reproduces the downward radiance field as resulting from a previous Monte Carlo run. The bottom boundary is either an infinitely thick absorbing layer, in which photons are lost from the system, or a Lambertian reflecting bottom of a given albedo, from which weighted photon packets are reflected.

After each collision, the weight of each photon packet is multiplied by the local value of  $\omega_0$  that is pertinent to the altitude or the depth, to account for its partial absorption. A packet history is terminated when its weight falls below a predetermined value, typically  $1 \times 10^{-6}$ . For each collision a random number on the unit interval is compared with the local value of the ratio of the molecular scattering coefficient to the total scattering coefficient to determine if the scattering event will be of molecular type (air or water molecules) or is due to an aerosol or hydrosol particle. The appropriate phase function is then used to determine the scattering angle; the orientation of the scattering plane is chosen at random on the interval  $(0, 2\pi)$ . The number of photons initiated depends on the single-scattering albedo value, so as to control the stochastic noise in the computed radiometric quantities (details can be found in Morel and Gentili<sup>31,32</sup>). The model is operated for its oceanic segment with the optical properties as specified in Section 3. For the atmospheric segment, fifty 1-km-thick layers are considered, with specified values for Rayleigh and aerosol scattering and for ozone absorption as in Elterman.<sup>19</sup> The aerosol phase function (as computed by Mie scattering theory) for the maritime aerosol model defined by the Radiation Commission of the International Association of Meteorology and Atmospheric Physics is used; see the models of Tanré *et al.*<sup>33</sup> and Baker and Frouin.<sup>34</sup>

#### F. Model MC4 [Monte Carlo 4 (Reinersman)]

This model is intended primarily for simulation of the radiance distribution above and just below the surface, and for simulation of irradiances with the first five mean free paths of the surface. The model is based on techniques described by Kirk.<sup>35</sup> The model atmosphere is composed of 50 layers, each characterized by separate Rayleigh and particulate scattering coefficients and an albedo of single scattering, as given by Elterman.<sup>19</sup> Weighted photon beams are projected into the atmosphere from the atmosphere-space boundary, and a collision is forced somewhere in the atmosphere along this original trajectory. The attenuated beam, which is the weight of the original beam less the portion lost to scattering and absorption, strikes the sea surface at the angle of the original trajectory. Beam losses that are due to absorption and scattering take place at the point of collision. There the absorbed portion is lost and the scattered portion exits the collision point in another single, weighted beam. A random number is compared with the ratio of the Rayleigh scattering cross

section to the total scattering cross section to determine the type of volume scattering function governing the scattering event. In the case of an aerosol scattering, a two-term Henyey–Greenstein phase function is used to determine the scattering angle.<sup>36</sup> Otherwise the angle is determined by a Rayleigh phase function.<sup>37</sup> Once the trajectory of the scattered portion of the beam is calculated, the distance from the point of collision to the next encountered interface (air–water or air–space) is determined. A new collision is forced somewhere along this trajectory, and the process is repeated until the weight of the scattered portion of the beam falls below a preset minimum fraction of the original beam weight. This minimum traceable weight is set to  $1 \times 10^{-6}$  of the original beam weight for the simulations presented below.

Some of the scattered trajectories encounter the atmosphere–space boundary and are forgotten; the others impinge on the sea surface. For the latter, the angle of incidence depends on the nadir angle of the ray and the slope of the sea surface. The directions of the reflected and refracted rays are determined geometrically, and the weights of the rays are calculated from the Fresnel formula. Although wave shadowing is neglected, multiple surface interactions may occur. A reflected ray that is still projected downward, or a transmitted ray that is still projected upward, must encounter the sea surface again immediately, without an intervening trajectory. Ray trajectories resulting from reflection are followed in the original manner. Transmitted portions of the beams are followed similarly until encountering the bottom or the sea surface, or until they are diminished to less than the minimum traceable weight. Those beams striking the bottom are lost; those beams that are incident upon the sea surface from below are again subjected to the reflection and transmission calculations.

#### G. Model MC5 [Monte Carlo 5 (Stavn)]

The Naval Research Laboratory optical model (referred to as the NORDA or NOARL optical model in earlier publications) uses standard Monte Carlo techniques.<sup>13,28,35</sup> At each scattering event, a random number is used to determine if the scattering is due to molecular water, quartzlike particulates, algae, or organic detritus; the volume scattering functions of these components are treated separately, rather than using an average volume scattering function. The model includes the effects of Raman scattering. If a photon collision results in inelastic scattering (as determined by comparing a random number to the appropriate optical properties of the medium), the wavelength is shifted by an amount corresponding to the mean wave-number shift of  $3357 \text{ cm}^{-1}$ , corresponding to Raman scatter by water molecules. The finite bandwidth of the Raman-shifted light is taken into account by averaging over 10-nm bandwidths (roughly corresponding to current oceanographic instruments); details of this averaging are described in

Stavn and Weidemann.<sup>38,39</sup> For the simulation of problem 7, below, it was assumed that the Raman scattering occurs in a very narrow waveband. The photons are tallied into zonal bands, as is convenient for computation of irradiances and the nadir-viewing radiance.

There is no atmosphere per se implemented in the model. Atmospheric transmittances of solar irradiance needed for simulations are obtained from the nonlayered atmospheric model of Brine and Iqbal.<sup>40</sup> The model determines the skylight radiance pattern from the empirical model of Harrison and Coombes.<sup>5</sup> The present version of the code handles only homogeneous waters.

### 3. Canonical Problems

We now define several canonical, or standard, problems for solution by underwater radiative transfer models. Models claiming to provide realistic simulations of the oceanic optical environment should be able to solve these problems and provide output that is at least as accurate as the data obtainable by presently available instrumentation. In brief, these problems are

- Problem 1: An unrealistically simple problem.
- Problem 2: A base problem using realistic inherent optical properties for the sea water.
- Problem 3: The base problem but with stratified water.
- Problem 4: The base problem but with atmospheric effects.
- Problem 5: The base problem but with a wind-blown sea surface.
- Problem 6: The base problem but with a finite-depth bottom.
- Problem 7: A problem involving Raman scattering.

In each of these problems, the water body is taken to be horizontally homogeneous. The real index of refraction of the water is  $n = 1.340$ . The depth below the surface can be specified by either the nondimensional optical depth  $\tau$  or by the geometric depth  $z$  in meters. The base problem 2 assumes that (a) the air–water surface is flat; (b) the water is homogeneous and infinitely deep; (c) there is no atmosphere, i.e., the sky is black; (d) the sun is a point light source located at a zenith angle of  $\theta_{\text{sun}} = 60^\circ$ ; (e) the sun provides a spectral irradiance just above the sea surface of magnitude  $E_{\perp} = 1 \text{ W m}^{-2} \text{ nm}^{-1}$  on a surface perpendicular to the sun's rays (which gives  $E_d = 0.5 \text{ W m}^{-2} \text{ nm}^{-1}$  for  $\theta_{\text{sun}} = 60^\circ$ ); (f) there is no inelastic scattering or other source of light within the water body; (g) the angular scattering properties of the water are characteristic of natural hydrosols; and (h) the water is either highly scattering ( $\omega_0 = 0.9$ ) or highly absorbing ( $\omega_0 = 0.2$ ). The other problems are defined by exceptions to these assumptions. The specific problem definitions are as follows.



### Problem 1. A Rayleigh phase function

$$\tilde{\beta}_w(\mu', \phi' \rightarrow \mu, \phi) \equiv \tilde{\beta}_w(\psi) = \frac{3}{16\pi} (1 + \cos^2 \psi) \quad (3)$$

is used to describe the angular scattering properties of the water. The scattering angle,  $\psi$ , is related to the incident  $(\mu', \phi')$  and scattered  $(\mu, \phi)$  directions by

$$\psi = \cos^{-1}[\mu\mu' + (1 - \mu^2)^{1/2}(1 - \mu'^2)^{1/2}\cos(\phi - \phi')].$$

This phase function, which is plotted in Fig. 1(b), is similar to that of pure sea water. The Rayleigh phase function is a well-behaved function of the scattering angle,  $\psi$ , and presents no numerical difficulties in its treatment; we therefore consider this an easy problem for numerical modeling. Note that  $\tilde{\beta}_w$  satisfies the normalization

$$2\pi \int_0^\pi \tilde{\beta}(\psi) \sin \psi d\psi = 1. \quad (4)$$

Both highly scattering ( $\omega_0 = 0.9$ ) and highly absorb-

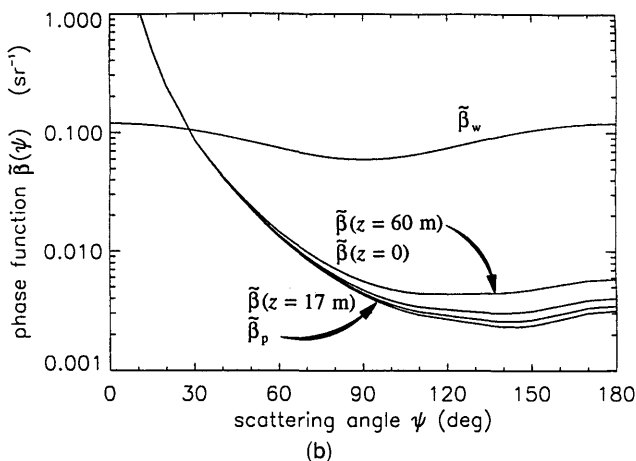
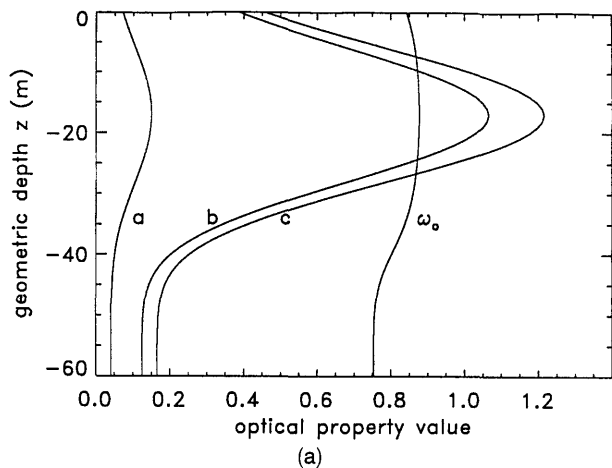


Fig. 1. (a) Inherent optical properties as a function of depth for problem 3. Coefficients  $a$ ,  $b$ , and  $c$  have units of inverse meters;  $\omega_0$  is dimensionless; (b) scattering-phase function for pure sea water,  $\tilde{\beta}_w$ ; for particles,  $\tilde{\beta}_p$ ; and for problem 3 at depths of  $z = 0, 17$ , and  $60$  m.

ing ( $\omega_0 = 0.2$ ) cases are considered for the Rayleigh phase function.

**Problem 2.** This base problem uses a phase function that is typical of oceanic waters. The total volume scattering function (VSF)  $\beta$  is

$$\beta = \beta_w + \beta_p,$$

where subscripts  $w$  and  $p$  refer to pure sea water and to particles, respectively. The total phase function  $\tilde{\beta}$  therefore can be expressed as

$$\tilde{\beta} = \frac{b_w}{b} \tilde{\beta}_w + \frac{b_p}{b} \tilde{\beta}_p. \quad (5)$$

This total  $\tilde{\beta}$  must satisfy the normalization (4), which is the case if  $\tilde{\beta}_w$  and  $\tilde{\beta}_p$  are each normalized.

The particle phase function,  $\tilde{\beta}_p$ , is defined from three VSF's measured by Petzold<sup>41</sup> in San Diego harbor. The VSF for pure sea water<sup>42</sup> was first subtracted to find the three particle VSF's. Then the scattering coefficient of pure sea water<sup>43</sup> ( $b_w = 0.00231 \text{ m}^{-1}$  at  $\lambda = 530 \text{ nm}$ , the wavelength of Petzold's data) was subtracted from the respective scattering coefficients computed by Petzold ( $b = 1.205, 1.536$ , and  $1.824 \text{ m}^{-1}$  for the three VSF's) to find the particle-scattering coefficient,  $b_p$ , for each VSF. The three particle phase functions were then computed with these  $b_p$ 's, and the mean value of the three  $\tilde{\beta}_p$ 's was computed at each scattering angle. This mean  $\tilde{\beta}_p(\psi)$  becomes infinite at  $\psi = 0$ , if it is assumed that  $\tilde{\beta}_p(\psi) \sim \psi^{-m}$  as  $\psi \rightarrow 0$ , where  $m = 1.346$  is the negative of the slope of  $\log \tilde{\beta}_p(\psi)$  versus  $\log \psi$  at the two smallest tabulated scattering angles ( $\psi = 0.10^\circ$  and  $0.12589^\circ$ ). When this functional form of  $\tilde{\beta}_p$  was used to integrate analytically  $2\pi\tilde{\beta}_p(\psi)\sin \psi$  from  $\psi = 0$  to  $\psi = 0.10^\circ$ , and the trapezoidal rule was used to integrate from  $\psi = 0.10^\circ$  to  $\psi = 180^\circ$ , the normalization integral (4) gave the value 1.006449. We thus divided the mean  $\tilde{\beta}_p$  by 1.006449 to obtain the values shown in Table 2. The particle phase function  $\tilde{\beta}_p(\psi)$  is then defined to be the tabulated values, with linear interpolation to be used between the tabulated values and with  $\tilde{\beta}_p(\psi) \equiv \tilde{\beta}_p(0.12589^\circ) (0.12589^\circ/\psi)^{1.346}$  for  $\psi < 0.12589^\circ$ . The resulting  $\tilde{\beta}_p(\psi)$  is defined for all  $\psi$  and exactly satisfies the normalization condition (4). This  $\tilde{\beta}_p$  is plotted in Fig. 1(b).

Moreover, because  $b_w = 0.00231 \text{ m}^{-1}$  is much less than  $b_p (> 1.2 \text{ m}^{-1})$  for each of the Petzold VSF's, it is reasonable to neglect the contribution of the water,  $\beta_w$ , to the total phase function of Eq. (5). This omission creates an error of at most a few percent in  $\beta$  even at backscattered directions ( $\psi > 90^\circ$ ). We therefore define the total phase function for problem 2 to be just the particle phase function as defined above:  $\tilde{\beta}(\psi) \equiv \tilde{\beta}_p(\psi)$ . This  $\tilde{\beta}$  is representative of phase functions measured in ocean waters with typical particle concentrations and, because of its highly peaked behavior at small  $\psi$ , can be expected to test the



**Table 2. Phase Function Values Used in Defining the Particulate Phase Function  $\beta_p(\psi)$**

Scattering Angle (deg)	Phase Function <sup>a</sup> (sr <sup>-1</sup> )	Scattering Angle (deg)	Phase Function (sr <sup>-1</sup> )
0.10000	1.76661+3	50.0	2.27533-2
0.12589	1.29564+3	55.0	1.69904-2
0.15849	9.50172+2	60.0	1.31254-2
0.19953	6.99092+2	65.0	1.04625-2
0.25119	5.13687+2	70.0	8.48826-3
0.31623	3.76373+2	75.0	6.97601-3
0.39811	2.76318+2	80.0	5.84232-3
0.50119	2.18839+2	85.0	4.95306-3
0.63096	1.44369+2	90.0	4.29232-3
0.79433	1.02241+2	95.0	3.78161-3
1.0000	7.16082+1	100.0	3.40405-3
1.2589	4.95803+1	105.0	3.11591-3
1.5849	3.39511+1	110.0	2.91222-3
1.9953	2.28129+1	115.0	2.79696-3
2.5119	1.51622+1	120.0	2.68568-3
3.1623	1.00154+1	125.0	2.57142-3
3.9811	6.57957	130.0	2.47603-3
5.0119	4.29530	135.0	2.37667-3
6.3096	2.80690	140.0	2.32898-3
7.9433	1.81927	145.0	2.31308-3
10.0	1.15257	150.0	2.36475-3
15.0	4.89344-1	155.0	2.50584-3
20.0	2.44424-1	160.0	2.66183-3
25.0	1.47151-1	165.0	2.83472-3
30.0	8.60848-2	170.0	3.03046-3
35.0	5.93075-2	175.0	3.09206-3
40.0	4.20985-2	180.0	3.15366-3
45.0	3.06722-2		

<sup>a</sup>The notation  $n \pm e = n \times 10^{\pm e}$ .

numerical models' abilities to handle realistic phase functions. Both highly scattering and highly absorbing cases are considered for this phase function.

**Problem 3.** This problem is designed to test the models' abilities to compute light fields in highly stratified water. The water stratification is specified as follows. The particulate absorption and scattering coefficients are taken to be

$$a_p = 0.04C^{0.602}, \quad (6a)$$

$$b_p = 0.33C^{0.620}, \quad (6b)$$

respectively, where  $C$  is the chlorophyll (pigment) concentration. When  $C$  is in milligrams per inverse meters cubed,  $a_p$  and  $b_p$  are in inverse meters. The absorption representation (6a) is based on Prieur and Sathyendranath<sup>44</sup> at a wavelength of  $\lambda = 500$  nm. The scattering representation (6b) is based on Gordon and Morel<sup>45</sup> with  $\lambda = 500$  nm and assuming that  $b_p(\lambda) \sim \lambda^{-1}$ . The pigment profile with depth is based on Lewis *et al.*<sup>46</sup> and consists of a Gaussian plus a constant background:

$$C(z) = C_0 + \frac{h}{s\sqrt{2\pi}} \exp\left[-\frac{1}{2}\left(\frac{z - z_{\max}}{s}\right)^2\right]. \quad (7a)$$

Platt and Sathyendranath<sup>47</sup> show that Eq. (7a) with

the parameter values

$$C_0 = 0.2 \text{ mg m}^{-3}, \quad (7b)$$

$$s = 9 \text{ m}, \quad (7c)$$

$$z_{\max} = 17 \text{ m}, \quad (7d)$$

$$h = 144 \text{ mg m}^{-2}, \quad (7e)$$

fits data from the Celtic Sea in May very well. We therefore adopt Eq. (7) as a reasonable model for  $C(z)$ . When Eq. (7) is used in Eq. (6), the particulate absorption and scattering coefficients, and hence all inherent optical properties, become functions of depth. The absorption and scattering coefficients for pure sea water at  $\lambda = 500$  nm are given by<sup>43</sup>

$$a_w = 0.0257 \text{ m}^{-1} \quad (8a)$$

$$b_w = 0.0029 \text{ m}^{-1}. \quad (8b)$$

When the chlorophyll concentration is low, scattering by pure sea water makes a significant contribution to the total scattering at large scattering angles (almost 1/2 when  $C = C_0$  and  $\psi = 180^\circ$ ). Therefore, for this problem it is necessary to use Eq. (5) to determine the total phase function from the phase functions for pure sea water,  $\beta_w$ , and for particles,  $\beta_p$ , as were defined in problems 1 and 2. The phase function is now a function of depth, as is the scattering-to-attenuation ratio

$$\omega_0 \equiv \frac{b}{c} = \frac{b_w + b_p(z)}{a_w + a_p(z) + b_w + b_p(z)}.$$

Figure 1(a) shows  $a$ ,  $b$ ,  $c$ , and  $\omega_0$  as functions of depth for problem 3, and Fig. 1(b) shows the phase functions at selected depths.

**Problem 4.** This problem is the same as problem 2 with  $\omega_0 = 0.9$ , except that atmospheric effects are included. The sky is no longer black but rather has a radiance distribution that describes the atmosphere's scattering and absorption effects on sunlight. The incident solar irradiance,  $E_\perp = 1 \text{ W m}^{-2} \text{ nm}^{-1}$ , is now applied at the top of the atmosphere. The atmospheric optical effects are defined by Elterman's<sup>19</sup> aerosol and Rayleigh-scattering optical thicknesses at  $\lambda = 500$  nm:

$$\tau_{\text{aerosol}} = 0.264,$$

$$\tau_{\text{Rayleigh}} = 0.145.$$

Because the numerical models incorporate atmospheric effects in various ways, a more detailed specification of the atmosphere is not made.

**Problem 5.** This problem is the same as problem 2 with  $\omega_0 = 0.9$ , except that the effects of a windblown sea surface are included. The surface waves are statistically specified as having a wave slope standard deviation of  $\sigma = 0.2$  in the Cox-Munk<sup>18</sup> capillary-

wave spectrum

$$\sigma^2 = 0.003 + 0.00512U,$$

where  $U$  is the wind speed in meters per second. Thus  $\sigma = 0.2$  corresponds to a wind speed of  $U = 7.23 \text{ m s}^{-1}$ . The solar zenith angle is taken to be  $\theta_{\text{sun}} = 80^\circ$ .

**Problem 6.** This problem is the same as problem 2, except that a finite-depth bottom is imposed. The bottom is taken to be an opaque, Lambertian reflecting surface at depth  $\tau = 5$ . This surface has an irradiance reflectance ( $E_u/E_d$ ) of 0.5. Such a surface is a reasonable model of a light-colored, sandy bottom.

**Problem 7.** This problem is for use in comparing models that include the effects of Raman scattering by water molecules. The wavelength of excitation is taken to be  $\lambda_{\text{ex}} = 417 \text{ nm}$ , and all light that is Raman scattered at 417 nm is assumed to shift to  $\lambda = 486 \text{ nm}$ . The Rayleigh phase function, Eq. (3), is used for elastic scattering. The phase function for Raman scattering is<sup>48</sup>

$$\tilde{\beta}_{\text{Ram}}(\psi) = \frac{3}{16\pi} \frac{1 + 3\rho}{1 + 2\rho} \left( 1 + \frac{1 - \rho}{1 + 3\rho} \cos^2 \psi \right), \quad (9)$$

where  $\rho$  is the depolarization ratio. For this problem, we use  $\rho = 0.17$  and take the total Raman scattering coefficient  $b_{\text{Ram}}$  equal to the elastic-scattering coefficient of the water itself, i.e.,  $b_{\text{Ram}} = b_w$ . The absorption and elastic-scattering coefficients of pure sea water at the wavelengths in question as taken from Smith and Baker<sup>43</sup> are

$$a_w(417) = 0.0156 \text{ m}^{-1},$$

$$b_w(417) = 0.0063 \text{ m}^{-1},$$

$$a_w(486) = 0.0188 \text{ m}^{-1},$$

$$b_w(486) = 0.0032 \text{ m}^{-1}.$$

Considering the way in which Smith and Baker

inferred  $a_w$  from irradiance data, it is assumed that  $b_{\text{Ram}}$  is already included in the value of  $a_w$ . Thus the total beam attenuation coefficient at each wavelength is just  $a_w + b_w$ . A unit irradiance  $E_\perp$  is incident at the sea surface upon a plane normal to the solar beam at the excitation wavelength  $\lambda_{\text{ex}} = 417 \text{ nm}$ . There is no atmosphere and no solar irradiance is incident upon the sea surface at  $\lambda = 486$ . The resulting irradiances at 486 nm are those that would be solely because of inelastic scattering from 417 nm. The solar zenith angle is  $60^\circ$  and the air–water surface is flat.

Table 3 summarizes the various canonical problems.

#### 4. Model Comparisons

Although the models generally compute the radiance  $L$ , the quantities most often used in oceanic optics are various irradiances. These irradiances are defined by weighted integrations of the radiance distribution over the upward and downward hemispheres of directions, as shown in Table 1, and are easily obtained from computed radiances. The nadir-viewing radiance,  $L_u$ , is the radiance seen by a sensor pointed straight down (in the nadir direction);  $L_u$  is important in remote-sensing studies. The ability of a numerical model to accurately compute the irradiances and nadir radiance is a measure of its utility for many oceanographic studies.

Models II and DO compute all quantities with equal accuracy. However, the Monte Carlo models MC1–MC5 compute upwelling quantities (e.g.,  $E_u$ ,  $E_{ou}$ , or  $L_u$ ) with less accuracy than downwelling quantities (e.g.,  $E_d$  or  $E_{od}$ ). This is because most of the simulated photons, all of which are initially heading downward, continue to head downward and thereby contribute to  $E_d$  or  $E_{od}$ . However, only the relatively few photons that are scattered into upward directions can contribute to  $E_u$ ,  $E_{ou}$ , or  $L_u$ ; fewer photons means greater statistical fluctuations in the computed values.

Also, for a given initial number of photons, the

Table 3. Summary of the Canonical Problems

Parameter	Problem						
	1 Easy Problem	2 Base Problem	3 Stratified Water	4 Atmospheric Effects	5 Windblown Surface	6 Bottom Effects	7 Raman Scattering
Albedo, $\omega_0$	0.9, 0.2	0.9, 0.2	Depth dependent	0.9	0.9	0.2	0.29 at 417 nm 0.15 at 486 nm
Phase function	Rayleigh Eq. (3)	Particle Table 2	Depth dependent	Particle Table 2	Particle Table 2	Particle Table 2	Eqs. (3) and (9)
Air–water surface	Flat	Flat	Flat	Flat	Capillary waves	Flat	Flat
Diffuse sky radiance	0	0	0	Various models	0	0	0
Internal sources	0	0	0	0	0	0	Various models
Bottom boundary	Infinitely deep	Infinitely deep	Infinitely deep	Infinitely deep	Infinitely deep	Lambertian at $\tau = 5$	Infinitely deep

Monte Carlo models must settle for less accuracy at a given optical depth  $\tau$  in highly absorbing waters (small  $\omega_0$ ) than in highly scattering waters (large  $\omega_0$ ). This is because photons absorbed before they reach depth  $\tau$  are not available to be tallied in the computation of the radiance or irradiance, whereas scattered photons can eventually reach depth  $\tau$  and be tallied. In practice, the accuracy of the Monte Carlo models is strongly dependent on the number of photon collisions; thus more photons must be processed when  $\omega_0$  is small to achieve satisfactory accuracy. The accuracy of models II and DO is independent of  $\omega_0$ .

With the above comments in mind, we selected  $E_d$ ,  $E_{ou}$ , and  $L_u$  for comparison just above the sea surface and at  $\tau = 1, 5$ , and  $10$ . Problems 1 and 2 have both highly scattering ( $\omega_0 = 0.9$ ) and highly absorbing ( $\omega_0 = 0.2$ ) waters.

Although it is not possible to compare the computa-

tional efficiencies of the various models because they were run on a variety of computers, with differing numbers of photons traced in the Monte Carlo codes, Table 4 shows some representative execution times. It should be noted that the long execution times shown for some of the Monte Carlo codes are the times required for accurate radiance simulations at large depths. If only irradiances or near-surface radiances are required for a particular study, these models can be run for much shorter times. For example, in the simulation of problem 3, output from model MC1 was compared for run times of 180 s and 7200 s. The  $E_d$  values throughout the euphotic zone (roughly the upper 21 m), as accumulated after 180 s, were within 1.5% of the values obtained after 7200 s. After 180 s, the  $E_{ou}$  and  $L_u$  values just below the surface (at  $z = 0$ ) were within 1% of their final values. Deeper within the euphotic zone,  $E_{ou}$  and  $L_u$  differed

Table 4. Representative Execution Times, and Numbers of Simulated Photons for Models MC1–MC5

Problem	Execution Time (s)	Number of Photons Initiated	Number of Photon Collisions
Model II (Computer: Sun SPARCstation 2, no code optimization)			
1, $\omega_0 = 0.9$	349 for $\tau = 10$ ; 730 for $\tau = 20$		
1, $\omega_0 = 0.2$	350 for $\tau = 10$ ; 733 for $\tau = 20$		
2, $\omega_0 = 0.9$	306 for $\tau = 10$ ; 496 for $\tau = 20$		
2, $\omega_0 = 0.2$	386 for $\tau = 10$ ; 711 for $\tau = 20$		
3	1180 for $z = 60$ m		
Model DO (Computer: Decstation 5000/240, no code optimization)			
1, $\omega_0 = 0.9$	5 for irradiances only, 2 layers		
1, $\omega_0 = 0.2$	5 for irradiances only, 2 layers		
2, $\omega_0 = 0.9$	9 for irradiances only, 2 layers; 435 for radiances, 2 layers		
2, $\omega_0 = 0.2$	9 for irradiances only, 2 layers		
3	171 for irradiances only, 25 layers		
Model MC1 (Computer: Decstation 5000)			
1, $\omega_0 = 0.9$	7200	$1.25 \times 10^6$	$4.98 \times 10^7$
1, $\omega_0 = 0.2$	7200	$6.63 \times 10^6$	$3.99 \times 10^7$
2, $\omega_0 = 0.9$	7200	$9.66 \times 10^6$	$7.18 \times 10^7$
2, $\omega_0 = 0.2$	7200	$7.17 \times 10^6$	$3.77 \times 10^7$
3	7200	$7.49 \times 10^6$	$8.74 \times 10^7$
Model MC2 (Computer: Vax 9000)			
1, $\omega_0 = 0.9$	5830	$1.0 \times 10^6$	$9.47 \times 10^7$
1, $\omega_0 = 0.2$	530	$1.0 \times 10^6$	$7.54 \times 10^7$
2, $\omega_0 = 0.9$	4630	$1.0 \times 10^6$	$9.72 \times 10^7$
2, $\omega_0 = 0.2$	410	$1.0 \times 10^6$	$7.85 \times 10^7$
Model MC3 (Computer: Hewlett Packard 9000/730)			
1, $\omega_0 = 0.9$	60000	$10.9 \times 10^6$	$6.72 \times 10^8$
1, $\omega_0 = 0.2$	74000	$55.7 \times 10^6$	$7.07 \times 10^8$
2, $\omega_0 = 0.9$	45000	$8.7 \times 10^6$	$7.30 \times 10^8$
2, $\omega_0 = 0.2$	84000	$63.7 \times 10^6$	$12.10 \times 10^8$
3	56000	$8.9 \times 10^6$	$9.02 \times 10^8$
Model MC4 (Computer: Microvax III)			
1, $\omega_0 = 0.9$	15100	$5.0 \times 10^4$	$1.66 \times 10^7$
1, $\omega_0 = 0.2$	17700	$1.0 \times 10^6$	$1.44 \times 10^7$
2, $\omega_0 = 0.9$	9680	$8.0 \times 10^4$	$1.24 \times 10^7$
2, $\omega_0 = 0.2$	10000	$1.2 \times 10^6$	$1.02 \times 10^7$
3	24200	$1.0 \times 10^5$	$3.06 \times 10^7$
Model MC5 (Computer: Cray Y-MP, no vectorization)			
1, $\omega_0 = 0.9$	1981 for $\tau = 20$	$1.0 \times 10^7$	
1, $\omega_0 = 0.2$	416 for $\tau = 10$	$1.0 \times 10^7$	
2, $\omega_0 = 0.9$	2300 for $\tau = 20$	$1.0 \times 10^7$	
2, $\omega_0 = 0.2$	389 for $\tau = 10$	$1.0 \times 10^7$	

by as much as 8% and 20%, respectively, for the two run times. At a depth of  $z = 60$  m, the differences in the computed quantities for the two times were 3% for  $E_d$ , 19% for  $E_{ou}$ , and a factor of six for  $L_u$ . Model DO is much more efficient for irradiance and nadir (or zenith) radiance computations, than for full radiance computations, because only the azimuthally averaged equation (i.e., the  $m = 0$  component of the radiance) is required to compute irradiances and nadir or zenith radiances. Full off-nadir or off-zenith radiance computations require the evaluation of additional azimuthal components. Strongly anisotropic scattering also requires a large number of streams.

We now briefly discuss the results of the models' simulations of problems 1–7.

**Problem 1.** Figure 2(a) shows the computed  $E_d$ ,  $E_{ou}$ , and  $L_u$  for the Rayleigh phase function of prob-

lem 1 and  $\omega_0 = 0.9$ . In this and subsequent figures, we plot the results from the two analytic models, II and DO, with solid lines; the Monte Carlo results are plotted with dashed lines. This makes it easy to see that, in most instances, the Monte Carlo results are distributed to either side of the analytic results, which are usually indistinguishable in the figures.

We first note in Fig. 2(a) that all models predict nearly the same values for a given quantity, although there is a detectable spread in  $L_u$  values that is due to Monte Carlo fluctuations. This behavior is expected, based on the preceding discussion. However, we also note that all models predict nearly the same values for  $E_d$  and  $E_{ou}$ , which is counter to intuition based on oceanographic experience. This result is easily explained if we recall that the Rayleigh phase function is nearly isotropic (independent of the scattering angle) and that the medium is highly scattering. Because of the intense scattering, the incident collimated radiance distribution approaches its asymptotic form very quickly with depth. Preisendorfer<sup>49</sup> shows that for an isotropic phase function the asymptotic radiance distribution,  $L_\infty$ , has an elliptical shape:

$$L_\infty(\theta) = \frac{L_0}{1 + k_\infty \cos \theta}. \quad (10)$$

Here  $L_0$  depends only on the inherent optical properties and  $k_\infty$  is the eccentricity of the ellipse;  $k_\infty$  is numerically equal to the nondimensional asymptotic diffuse attenuation coefficient. The analytic forms of  $L_\infty$  for a Rayleigh phase function and a Rayleigh phase matrix are also known.<sup>50</sup> For  $\omega_0 = 0.9$  the Rayleigh  $L_\infty$  is very close to elliptical, and so we can use the simpler form of Eq. (10) for the following argument. The  $E_d$  and  $E_{ou}$  corresponding to  $L_\infty$  of Eq. (10) are

$$E_d = -\frac{2\pi L_0}{k_\infty^2} [k_\infty + \ln(1 - k_\infty)],$$

$$E_{ou} = \frac{2\pi L_0}{k_\infty} \ln(1 + k_\infty). \quad (11)$$

Now the value of  $k_\infty$  for the problem at hand turns out to be  $k_\infty \approx 0.52$  (see Table 7). This value is coincidentally very near to the value  $k_\infty = 0.531$ , which makes  $E_d = E_{ou}$  in Eq. (11), thus explaining the numerical results seen in Fig. 2(a). This peculiar behavior of  $E_d$  and  $E_{ou}$  depends on both the phase function and the scattering-to-attenuation ratio. Such behavior is not seen in the output for the other problems, nor would it ever be encountered in a natural water body.

Note also that both  $E_d$  and  $E_{ou}$  are greater just below the water surface than just above it, which may also seem counterintuitive. However, this is just the phenomenon of optical energy trapping in highly scattering waters, as discussed by Stavn *et al.*<sup>51</sup> and by Plass *et al.*<sup>52</sup> In the present case of a solar angle of  $60^\circ$ , more than 93% of the incident solar irradiance is transmitted through the level surface into the water. Approximately one half of the highly diffuse

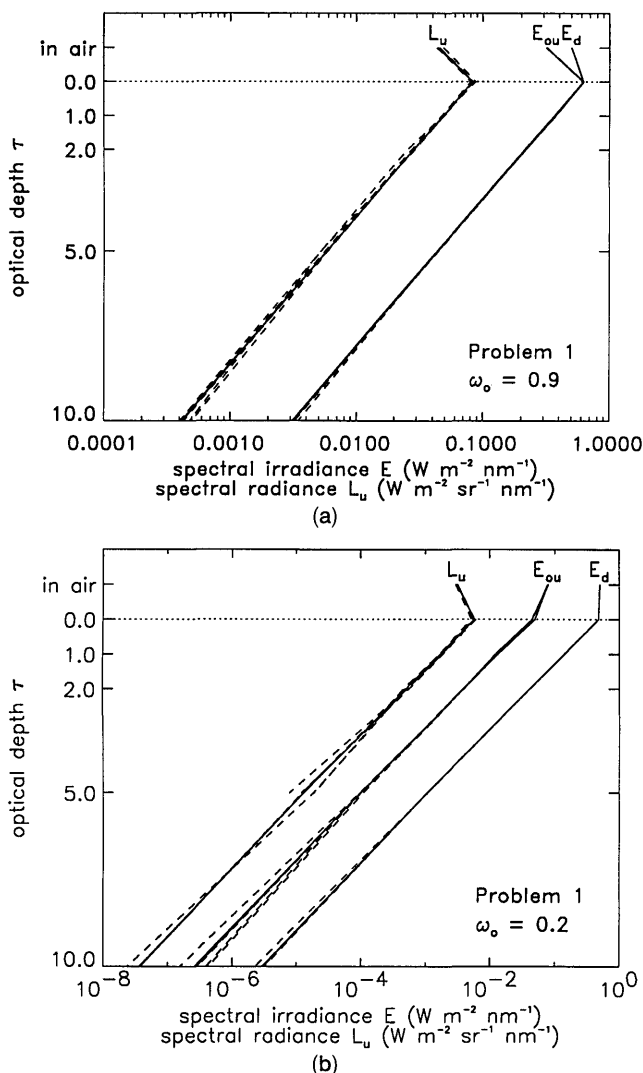


Fig. 2. (a)  $E_d$ ,  $E_{ou}$ , and  $L_u$  as computed by the various models for problem 1,  $\omega_0 = 0.9$ ; (b) the same quantities as computed for the case of  $\omega_0 = 0.2$ . The dotted line represents the air–water surface. Results from models II and DO are plotted with solid lines; models MC1–MC5 are plotted with dashed lines. Depth  $\tau = 0$  is in the water, just below the surface, and in air represents a point just above the surface.

upwelling irradiance just below the surface is reflected back down by the surface. The total  $E_d$  just below the surface is the sum of the transmitted solar contribution and the reflected upwelling contribution; this sum is greater than  $E_d(\text{air})$ . Likewise,  $E_{ou}(\text{air})$  consists of the (relatively weak) specularly reflected solar beam plus diffuse light transmitted upward through the water surface; this sum is less than  $E_{ou}$  just below the surface.

Figure 2(b) shows the output for the Rayleigh phase function and a highly absorbing medium with  $\omega_0 = 0.2$ . Now  $E_{ou}$  is an order of magnitude less than  $E_d$ . There is a spread of almost a factor of 3 in the Monte Carlo estimates of  $E_{ou}$  at  $\tau = 10$ , and three of the Monte Carlo models had too few photons left at  $\tau = 10$  to provide an estimate of  $L_u$  at that depth. This behavior is expected for this highly absorbing case.

Table 5 displays the average (over all models) values of  $E_d$ ,  $E_{ou}$ , and  $L_u$  at selected depths for this and the remaining problems. These data are provided for readers who wish to compare their own models with ours. Such comparisons should be especially worthwhile for simple parameterized models that attempt to compute irradiances without solving the complete radiative transfer equation. Table 5 also displays the ratio of the sample standard deviation  $s$  to the sample mean  $\bar{x}$ ,

$$\frac{s}{\bar{x}} = \frac{\left[ \frac{1}{N-1} \sum_{i=1}^N (x_i - \bar{x})^2 \right]^{1/2}}{\frac{1}{N} \sum_{i=1}^N x_i},$$

where  $x_i$  is the result predicted by the  $i$ th model for the quantity of interest and  $N$  is the number of model predictions ( $N = 7$  for most quantities). The ratio  $s/\bar{x}$  is a quantitative measure of how close together the models' predictions are for a given quantity. Inspection of this ratio for problem 1 shows that the model predictions are usually closer together for the highly scattering case ( $\omega_0 = 0.9$ ) than for the highly absorbing case ( $\omega_0 = 0.2$ ), closer together at shallow depths, and closest together for  $E_d$ . The greatest spread in values is for  $L_u$  at large depths, because of the small number of photons available for its estimation by the Monte Carlo models.

**Problem 2.** Figure 3 shows the models' output for problem 2. Figure 3(a) is for the highly scattering case of  $\omega_0 = 0.9$ . Each of the seven models provides essentially the same values for  $E_d$  and for  $E_{ou}$  to 10 optical depths (and deeper); some Monte Carlo fluctuation is apparent in the  $L_u$  values. Figure 3(b) shows the same computations for the highly absorbing case of  $\omega_0 = 0.2$ . Once again, all models give nearly the same values for  $E_d$  and for  $E_{ou}$  to 10 optical depths. Now, however, considerable Monte Carlo fluctuation in the  $L_u$  values is seen at even shallow depths; only models II, DO, and MC3 were able to compute  $L_u$  below  $\tau = 10$ .

We emphasize that the large fluctuations seen in some of the estimates in Fig. 3(b) are simply the result of tracing an insufficient number of photons in the simulations, and not of any inadequacies in the models themselves. Tracing additional photons, at a proportional increase in computational expense, can reduce these fluctuations to any desired level. The particular values seen in Fig. 3 are each the result of one simulation. Running the Monte Carlo models with different seeds for their random number generators would generate a noticeably different set of curves for those instances where large fluctuations are seen in Fig. 3. It should be noted that there are certain sampling schemes that can improve the statistics at greater depths. However, this improvement is usually at the expense of larger errors in the radiometric quantities at smaller depths.

The euphotic zone is the region of a water body

Table 5. Average Values of  $E_d$ ,  $E_{ou}$ , and  $L_u$  at Selected Depths for Problems 1-6<sup>a</sup>

Optical Depth	Average Value			Corresponding $s/\bar{x}$		
	$E_d$	$E_{ou}$	$L_u$	$E_d$	$E_{ou}$	$L_u$
Problem 1, $\omega_0 = 0.9$ ( $N = 7$ )						
1	3.66-1	3.72-1	4.85-2	0.002	0.005	0.015
5	4.33-2	4.35-2	5.59-3	0.003	0.007	0.052
10	3.16-3	3.20-3	4.37-4	0.015	0.038	0.091
Problem 1, $\omega_0 = 0.2$ ( $N = 7$ )						
1	1.41-1	1.34-2	1.72-3	0.001	0.003	0.044
5	1.07-3	1.00-4	1.37-5	0.005	0.039	0.288
10	2.93-6	3.00-7	3.39-8 ( $N = 4$ )	0.102	0.308	0.197
Problem 2, $\omega_0 = 0.9$ ( $N = 7$ )						
1	4.13-1	9.31-2	6.99-3	0.001	0.021	0.063
5	1.87-1	4.63-2	3.26-3	0.005	0.017	0.055
10	6.85-2	1.65-2	1.21-3	0.010	0.014	0.109
Problem 2, $\omega_0 = 0.2$ ( $N = 7$ )						
1	1.62-1	9.66-4	5.47-5	0.000	0.023	0.060
5	2.27-3	1.37-5	6.24-7 ( $N = 6$ )	0.002	0.063	0.355
10	1.30-5	7.28-8	4.02-9 ( $N = 5$ )	0.047	0.187	0.248
Problem 3 ( $N = 6$ )						
5 m	2.30-1	4.34-2	3.13-3	0.006	0.025	0.054
25 m	1.62-3	2.86-4	2.12-5	0.028	0.038	0.061
60 m	5.23-5	5.13-6	3.57-7	0.071	0.036	0.434
Problem 4 ( $N = 6$ ) <sup>b</sup>						
1	3.23-1	7.13-2	5.63-3	0.076	0.091	0.111
5	1.49-1	3.57-2	2.77-3	0.072	0.076	0.141
10	5.56-2	1.31-2	9.60-4	0.070	0.073	0.107
Problem 5 ( $N = 4$ )						
1	1.14-1	3.55-2	2.09-3	0.012	0.020	0.031
5	4.33-2	1.22-2	7.63-4	0.009	0.028	0.036
10	1.48-2	3.65-3	2.49-4	0.007	0.020	0.025
Problem 6 ( $N = 3$ )						
1	1.62-1	9.81-4	6.84-5	0.000	0.010	0.020
5	2.28-3	2.28-3	3.60-4	0.003	0.002	0.010

<sup>a</sup> $N$  is the number of models included in the averages. The ratio of the sample standard deviation to the sample mean,  $s/\bar{x}$ , is also displayed for each average value. The average values are relative to an incident solar irradiance of  $E_{\perp} = 1.0 \text{ W m}^{-2} \text{ nm}^{-1}$  upon the water surface, except for problem 4, for which  $E_{\perp}$  is applied at the top of the atmosphere. The notation 3.66-1, for example, means  $3.66 \times 10^{-1}$ .

<sup>b</sup> $s/\bar{x}$  values determined by systematic offset; see discussion in the text.

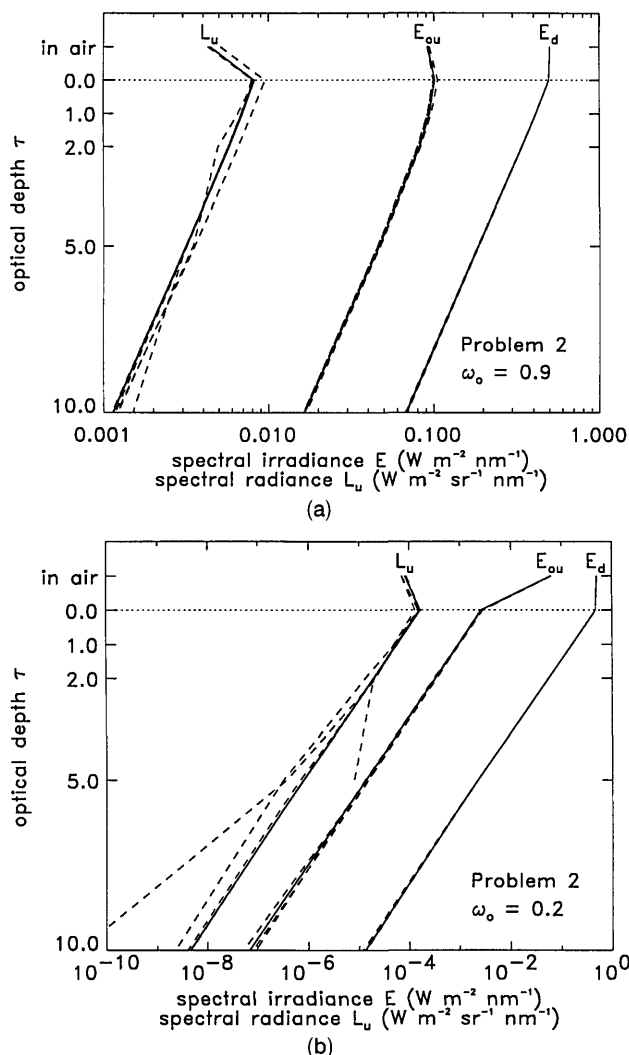


Fig. 3. Model predictions for problem 2, the base case: (a)  $\omega_0 = 0.9$  and (b)  $\omega_0 = 0.2$ .

where there is sufficient light for photosynthesis to take place. In normal daylight conditions, it extends from the surface to a depth where the irradiance is roughly 1% of its surface value. We see in Fig. 3(b) that  $E_d$  and  $E_{ou}$  have decreased by 2 orders of magnitude at approximately 4 optical depths. Each of the models produces nearly identical irradiances to depths greater than  $\tau = 4$ , so that each of the models is perfectly adequate for the purposes of biological oceanography. Likewise, the models produce very nearly the same water-leaving radiances,  $L_u(\text{air})$ , as would be of interest in remote-sensing studies.

**Problem 3.** Figure 4 shows the models' output for problem 3, the stratified water case. The 1% irradiance level is now at approximately  $z = 21$  m. Once again, the models provide nearly identical output to depths far below the euphotic zone.

**Problem 4.** Figure 5 shows  $E_d$  values near the water surface for the simulation of problem 4, the case with an atmosphere. The different ways in which the models simulate the atmosphere lead to an 18% spread in the values of  $E_d$  just above the water

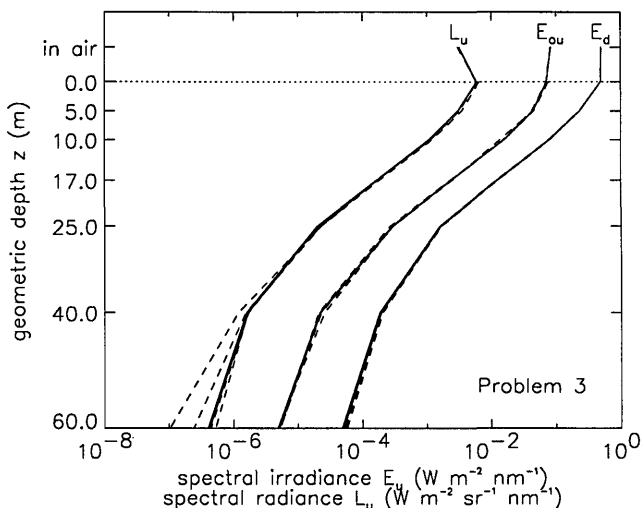


Fig. 4. Model predictions for problem 3, the stratified-water case.

surface. This difference in  $E_d(\text{air})$  values is then carried throughout the underwater computations. The  $s/\bar{x}$  ratio displayed in Table 5 is uniformly large for this problem because of the systematic offset of the different models' predictions. Note that apparent optical properties, such as reflectances and diffuse attenuation functions, are not affected by this offset, because the apparent properties are defined as ratios of radiometric quantities. For example, the  $s/\bar{x}$  ratio for the  $K_d$  values computed from the plotted  $E_d$  values at depths  $z = 0$  and 1 m is 0.009, which is much smaller than the  $s/\bar{x} = 0.076$  value tabulated for  $E_d$  at  $\tau = 1$ .

**Problem 5.** Four of the models (II, MC1, MC3, and MC4) are capable of simulating a windblown air-water surface as defined in problem 5. Figure 6 shows output from these models for a solar zenith angle of  $\theta_{\text{sun}} = 80^\circ$ . The models are nearly identical in their output, even in this case of nearly horizontal incidence, for which any differences in the models should be most noticeable. Note that  $E_{ou}(\text{air})$  is

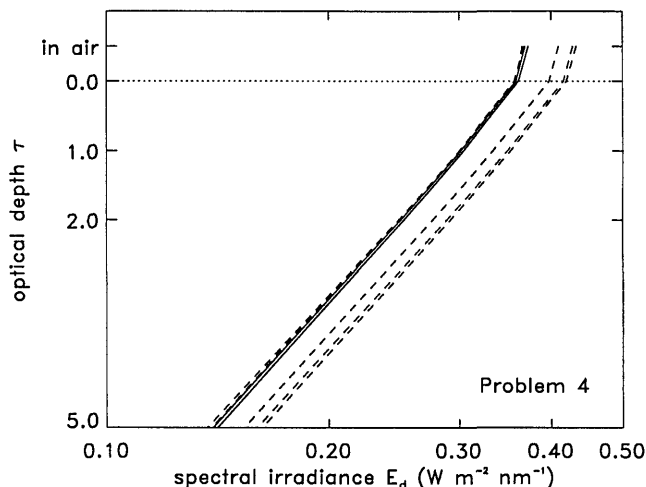


Fig. 5.  $E_d$  near the surface for problem 4, the base case plus an atmosphere.

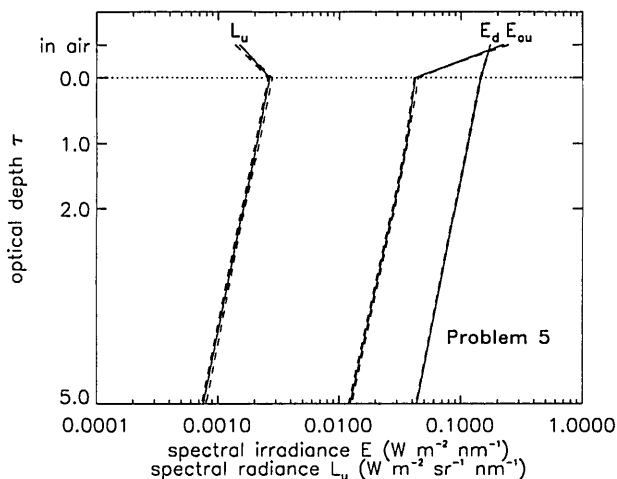


Fig. 6. Model predictions near the surface for problem 5, the capillary-wave case. The wind speed is  $U = 7.23 \text{ m s}^{-1}$ , and the zenith angle of the sun is  $\theta_{\text{sun}} = 80^\circ$ .

greater than  $E_d(\text{air})$ . This is because  $E_{ou}(\text{air})$  contains a large contribution by the specularly reflected solar beam: simulations by Preisendorfer and Mobley<sup>4</sup> show that the reflectance of a capillary-wave surface is greater than 0.22 for a wind speed of  $7.23 \text{ m s}^{-1}$  and  $\theta_{\text{sun}} = 80^\circ$ . The solar beam contribution to  $E_d$  is weighted by a  $\cos \theta_{\text{sun}}$  factor, which is small for  $\theta_{\text{sun}} = 80^\circ$ .

**Problem 6.** Models II, DO, and MC3 can simulate a finite-depth bottom. Figure 7 shows the output from both models for the case of  $\omega_0 = 0.2$ ; the models are clearly in excellent agreement. It is easy to show that  $E_{ou} = E_d$  for a Lambertian surface of reflectance 0.5, and all three models show this expected result at depth  $\tau = 5$ .

**Problem 7.** Four of the models (MC1, MC2, MC3, and MC5) can simulate Raman scattering. Table 6 compares the inelastically scattered contributions to the downwelling and upwelling plane irradiances,  $E_d$  and  $E_u$ , respectively, for the simulation defined in

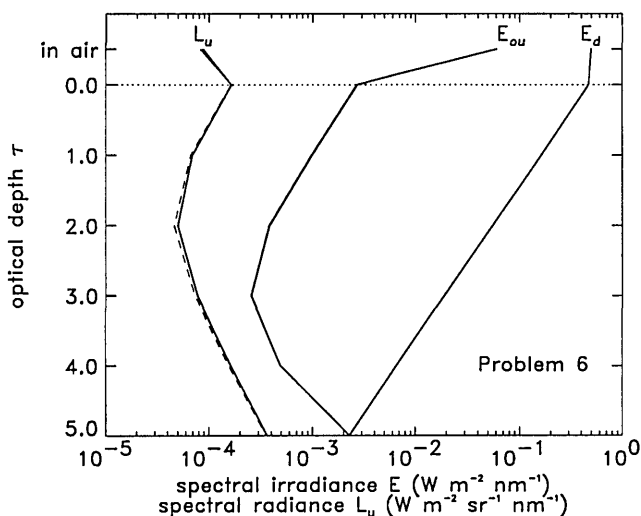


Fig. 7. Model predictions for problem 6, the finite-depth case. The bottom reflectance is 0.5.

Table 6. Raman Scattering Contributions to  $E_d$  and  $E_u$  at  $\lambda = 486 \text{ nm}$  From an Excitation Wavelength of  $\lambda_{\text{ex}} = 417 \text{ nm}$ <sup>a</sup>

Depth (m)	Model			
	MC1	MC2	MC3	MC5
<i>E<sub>d</sub></i> values				
0	0.01875	0.01874	0.01739	0.01873
50	0.02489	0.02488	0.02470	0.02490
100	0.01136	0.01136	0.01123	0.01138
<i>E<sub>u</sub></i> values				
0	0.03532	0.03512	0.03478	0.03523
50	0.01034	0.01042	0.01027	0.01039
100	0.00287	0.00296	0.00292	0.00296

<sup>a</sup>Parameter values are given in the specification of problem 7. Values in the body of the table have units of  $\text{W m}^{-2} \text{ nm}^{-1}$  for an incident irradiance of  $E_{\perp} = 1.0 \text{ W m}^{-2} \text{ nm}^{-1}$  at  $\lambda_{\text{ex}}$ .

problem 7. The models are clearly in excellent agreement, even though their respective formulations of inelastic scatter are somewhat different.

**Computation of radiance distributions.** Five of the models (II, DO, MC2, MC3, and MC4) compute the full radiance distribution, rather than just tallying photons as necessary to compute the irradiances and  $L_u$ . Figure 8 illustrates the consistency with which the various models compute the radiance distribution. The figure shows  $L(\tau, \theta, \phi)$  in the plane of the sun at depths of  $\tau = 0, 5$ , and  $20$  for problem 2,  $\omega_0 = 0.9$ . Direction  $(\theta_v, \phi_v)$  gives the viewing direction, i.e., the direction an instrument points to detect photons traveling in the  $(\theta = 180^\circ - \theta_v, \phi = 180^\circ + \phi_v)$  direction. Thus  $\theta_v = 180^\circ$  corresponds to looking straight up and seeing photons heading straight down; the nadir radiance,  $L_u$ , of Fig. 3(a) is the value plotted at  $\theta_v = 0^\circ$ . The sun is in the  $\phi_v = 0^\circ$  half-plane.

The curves of Fig. 8 are explained as follows. We begin at  $\tau = 0$  (in the water just below the surface)

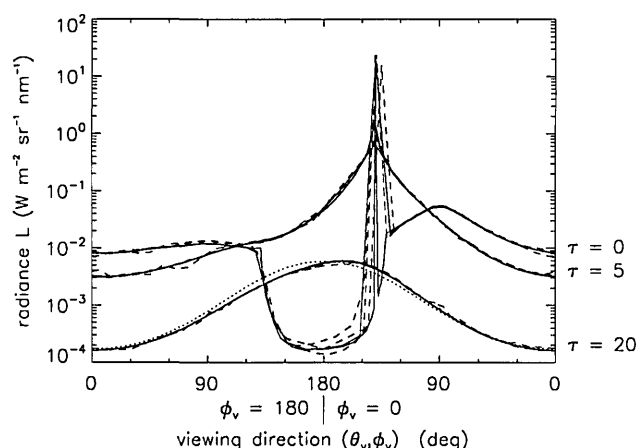


Fig. 8. Radiance distribution in the plane of the sun for problem 2,  $\omega_0 = 0.9$ . Angles  $(\theta_v, \phi_v)$  are viewing directions:  $\theta_v = 180^\circ - \theta$  and  $\phi_v = 180^\circ + \phi$ , where  $(\theta, \phi)$  are the directions of photon travel. The solid curves are  $L(\tau, \theta_v, \phi_v)$  at selected depths within the water for models II and DO; models MC2–MC4 are shown by the dashed curves. The dotted curve is the asymptotic distribution  $L_{\infty}(\theta_v)$  normalized to the largest value of  $L$  at  $\tau = 20$ .



with our backs to the sun (looking in the  $\phi_v = 180^\circ$  direction). Looking straight down we see the nadir radiance at  $(\theta_v, \phi_v) = (0^\circ, 180^\circ)$ . Looking up toward the horizontal ( $\theta_v = 90^\circ$ ), the radiance increases slightly because of total internal reflection of radiance that has been scattered into nearly horizontal directions. The radiance then decreases quickly as our viewing angle passes beyond the critical angle for total internal reflection. In the region around  $\theta_v = 180^\circ$  we are looking upward and seeing the upwelling radiance that is reflected downward by the level water surface. Note for example (using the digital output from Model II) that  $L(\tau = 0, \theta_v = 180^\circ)/L(\tau = 0, \theta_v = 0^\circ) = 1.737 \times 10^{-4}/8.236 \times 10^{-3} = 0.021$ , which is just the Fresnel reflectance of the surface for perpendicular incidence. Recall that in problem 2 the sky is black, so there is no sky radiance transmitted through the surface. In problem 4 (not shown), transmitted sky radiance fills in the large dip in the radiance near  $\theta_v = 180^\circ$ . As our view passes the zenith we are now facing the sun. The large spike in the radiance near  $(\theta_v, \phi_v) = (140^\circ, 0^\circ)$  is the refracted solar beam. The noticeable  $\theta_v$  offset in the position of the plotted peak radiance occurs because different models choose their quad boundaries differently. The radiance values are plotted at the  $\theta_v$  values of the quad centers, which range from  $135^\circ$  to  $139.7^\circ$  for the quad containing the refracted solar beam; plotted points are connected by straight lines. Looking beyond the sun, we see a large horizontal radiance, which decreases as we look downward.

Model DO shows a more pronounced spike in the radiance near the solar direction, and more pronounced changes near the critical angle than do the other models. This is because model DO computes radiances in specific directions, rather than quad-averaged radiances. The angular quadrature points in model DO are clustered near the critical angle and near the horizon, to get increased resolution in regions where the radiance varies rapidly with polar angle.

By depth  $\tau = 5$ , scattering has smeared out the solar beam and increased the downwelling radiance seen when looking upward near the zenith. The radiance distribution at  $\tau = 20$  is very similar in shape to the asymptotic distribution,  $L_\infty(\theta_v)$ . The asymptotic distribution as computed by model II and normalized to the largest value of  $L(\tau = 20)$  is shown as a dotted line in Fig. 8. Note that only a small amount of Monte Carlo fluctuation is seen even at  $\tau = 20$ , for this highly scattering case.

Radiance distributions computed by the various models are in equally close agreement for the other canonical problems (except for Monte Carlo fluctuations in the small  $\omega_0$  cases) and will not be discussed.

**Computation of asymptotic radiances.** The asymptotic radiance regime (also called the diffusion regime) is the region far enough from the boundaries of a homogeneous medium that the radiance is independent of the incident direction of the source and of boundary effects. Radiance in the asymptotic re-

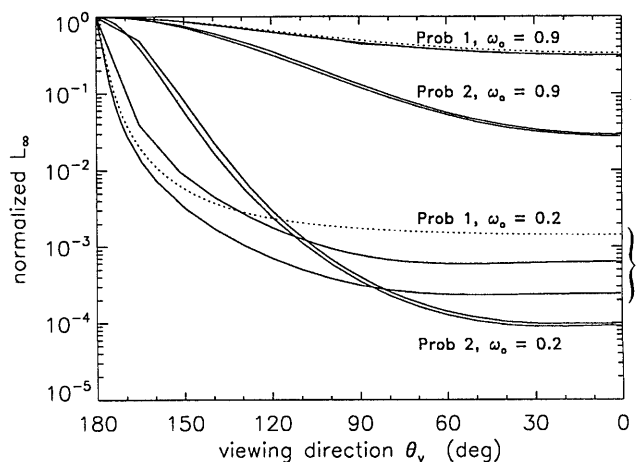


Fig. 9. Asymptotic radiance distributions  $L_\infty(\theta_v)$  for problems 1 and 2, as computed by various models (solid curves). The dotted curves give the exact analytic solution<sup>46</sup> for the Rayleigh phase function of problem 1.

gime is independent of the azimuthal angle  $\phi$ , and it decreases exponentially as  $\exp(-k_\infty \tau)$ . Here  $k_\infty = K_\infty/c$ , where  $K_\infty$  is the dimensional (in inverse meters) asymptotic diffuse attenuation coefficient and  $c$  is the beam attenuation coefficient. The shape  $L_\infty(\theta)$  of the asymptotic radiance distribution is determined only by the inherent optical properties of the water; it is independent of depth.

Model II computes  $L_\infty(\theta)$  and the associated value of the nondimensional asymptotic diffuse attenuation coefficient  $k_\infty$  by the solution of a matrix eigenvalue equation.<sup>6</sup> The smallest eigenvalue of the matrix is  $k_\infty$ , and the associated eigenvector gives  $L_\infty$ . Model DO obtains the asymptotic solution in a similar fashion. Models MC2 and MC3 obtain  $L_\infty$  and  $k_\infty$  by solution of the equivalent integral equation<sup>49,53</sup>

$$(1 - k_\infty \mu) L_\infty(\mu) = \omega_0 \int_0^{2\pi} \int_{-1}^1 L_\infty(\mu') \tilde{\beta}(\psi) d\mu' d\phi'. \quad (12)$$

The exact analytical solution to Eq. (12) for the case of scattering according to a Rayleigh phase function, as well as for a Rayleigh phase matrix, was found by Kattawar and Plass.<sup>50</sup> Numerical solutions for phase functions that are highly peaked in the forward direction have been given in Kattawar and Plass<sup>50</sup> and in Prieur and Morel.<sup>54</sup>

Figure 9 shows the computed  $L_\infty(\theta_v)$ , normalized to one at  $\theta_v = 180^\circ$ , for problems 1 and 2. Table 7

Table 7. Computed Values of  $k_\infty$ .

Problem	Model				
	II	DO	MC1 <sup>a</sup>	MC2	MC3
1, $\omega_0 = 0.9$	0.5248	0.5232	0.52	0.5232	0.5235
1, $\omega_0 = 0.2$	1.0006	0.9994	—	0.9996	0.9952
2, $\omega_0 = 0.9$	0.1920	0.2068	0.189	0.1835	0.1879
2, $\omega_0 = 0.2$	0.8737	0.8794	—	0.8590	0.8619

<sup>a</sup>Values determined by visual inspection of plotted output.

**Table 8. Comparison of Percent Accuracies for Computing and Measuring Radiometric Variables**

Variable	2 $\sigma$ Spread of Model Values	Current Measurement Capability	Target Accuracy for SeaWiFS <sup>a</sup>
$E_d$	1	3–5	2
$E_{ou}$	5	3–5	—
$L_u$	12	3–5	3

<sup>a</sup>From Mueller and Austin.<sup>55</sup>

shows the corresponding  $k_\infty$  values. The numerical results are in excellent agreement for problem 2 and for the  $\omega_0 = 0.9$  case of problem 1, which also agrees with its exact analytic solution. However, the numerical results differ considerably for the  $\omega_0 = 0.2$  case of problem 1, and each is considerably off from the analytic solution. The reason for this inaccuracy in the computed  $L_\infty$  is as follows. For problem 1,  $\omega_0 = 0.2$ , the analytic  $k_\infty$  value is  $k_\infty \approx 0.99937$ . However, Eq. (12) becomes singular as  $\mu \rightarrow 1$  when  $k_\infty = 1$ . For the nearly singular case at hand, both model II's eigenmatrix routine and the integral equation routines are having a difficult time determining accurate values for  $k_\infty$  and  $L_\infty$ . This is most noticeable in the  $k_\infty = 1.0006$  value determined by model II; the theoretical upper limit for  $k_\infty$  is exactly one. Even slight errors in  $k_\infty$  cause large differences in  $L_\infty$  when  $k_\infty$  is near one. Kattawar was able to obtain a satisfactory numerical solution of Eq. (12) for this case only after resorting to quadruple-precision arithmetic. The  $k_\infty \approx 0.87$  value seen in problem 2,  $\omega_0 = 0.2$ , is far enough from one that no numerical difficulties arise. Note that the computation of  $k_\infty$  and  $L_\infty$  is a separate problem from the computation of the radiances and irradiances as discussed above. The inaccuracies in  $k_\infty$  and  $L_\infty$  just discussed in no way imply inaccuracies in the solution of Eq. (1).

## 5. Conclusions

Problems 1–3 of Section 3 cover the extreme range of oceanic inherent optical properties:  $\omega_0$  from 0.2 to 0.9, phase functions for pure Rayleigh and pure particulate scattering, and strong vertical stratification. In computations of  $E_d$  and  $E_{ou}$ , the numerical models of Section 2 usually gave results within a few percent of each other throughout the euphotic zone. The spread in  $L_u$  values was as large as 12% in highly scattering waters and much larger in highly absorbing waters at the bottom of the euphotic zone.

The statistical fluctuations of the Monte Carlo results from the true values of the predicted quantities are normally distributed. We therefore expect that more than 95% of the Monte Carlo simulations will be within 2 standard deviations ( $2\sigma$ ) of the correct value. The data of Table 5 give us a feeling for the size of this  $2\sigma$  spread of values. Table 8 shows the  $2\sigma$  spread (expressed as a percentage of the mean) for  $E_d$ ,  $E_{ou}$ , and  $L_u$  in near-surface waters (based on  $\tau = 1$  for problems 1 and 2 and based on  $z = 5$  m for problem 3). Column 2 of Table 8 shows typical errors in these

radiometric quantities when measured by commercial instruments now in wide use. The third column of the table shows the accuracy desired in measurements to be used for ground-truth validation of the SeaWiFS ocean color satellite<sup>55</sup> (to be launched in 1994). Obtaining such accuracies in  $E_d$  and  $L_u$  measurements requires very careful instrument calibration.

We see from Table 8 that the present numerical models easily compute  $E_d$  with greater accuracy than can be obtained with current instruments. Numerical estimates of  $E_{ou}$  have approximately the same accuracy as measured values. The computed values of  $L_u$  are less accurate than can be measured or than are needed for remote-sensing studies requiring absolute radiometric values of  $L_u$ . Thus the Monte Carlo models should trace more photon histories, if very accurate  $L_u$  values are required. The standard deviation of the Monte Carlo fluctuations is proportional to  $n^{-1/2}$ , where  $n$  is the number of photons traced. Therefore the  $2\sigma$  spread seen in Table 8 can be cut in half by tracing four times as many photons, which is computationally practicable. Another possibility is to use the backward Monte Carlo method, as described in Gordon.<sup>56</sup>

Monte Carlo calculations made using statistical estimation techniques can also yield continuum radiances, rather than quad-averaged values. Thus if one is interested in results for a few detectors located at precise angles, this technique can give highly accurate radiance values with only a very few photons being traced.<sup>57–59</sup>

Values predicted by the Monte Carlo models generally fall on both sides of the values predicted by models II and DO, which do not have statistical fluctuations. Thus models II and DO have an advantage in the computation of upwelling quantities or in computations at great depths, which require tracing very large numbers of photons in the Monte Carlo codes.

The systematic differences in the atmospheric models used to simulate problem 4 lead to a  $2\sigma$  spread of the order of 20% in the computed radiometric quantities. Thus to compute acceptably accurate absolute radiometric values, more careful attention must be paid to how the incident radiance upon the water surface is obtained. However, as noted before, systematic offsets in the absolute radiometric variables do not affect the values of apparent optical properties obtained from the radiometric variables. The present simple atmospheric models therefore all appear to be satisfactory for the computation of apparent optical properties.

Based on the problem solutions presented above, and on such comparisons between models and oceanographic measurements as have been made (not discussed here), we conclude that each of the numerical models discussed here incorporates correct mathematical representations of the relevant radiative processes (absorption and elastic and inelastic scattering) and of the effects of the air–water boundary.

Moreover, the models provide accurate numerical solutions of the associated equations. Each of these models is adequate for most of the needs of optical oceanography and limnology.

#### Appendix A: Inelastic Source Function for Model MC1

As noted in Section 2, model MC1 incorporates Raman scattering (and other inelastic processes, such as fluorescence) in an azimuthally averaged form suitable for the computation of inelastic-scattering effects on irradiances. The corresponding mathematical form of the source function, which is used in the  $\phi$ -averaged version of Eq. (1), is developed as follows. This formulation is based on expanding both the Raman scattering function and the azimuthally averaged excitation radiance in a series of Legendre polynomials.<sup>60</sup>

The source function for inelastic processes is given by

$$S_{\text{in}}(z, \theta, \lambda) = \frac{1}{4\pi} \sum_{l=0}^N \int b_{\text{in}}^{(l)}(z, \lambda_{\text{ex}} \rightarrow \lambda) P_l(\cos \theta) E_l(z, \lambda_{\text{ex}}) d\lambda_{\text{ex}},$$

with

$$E_l(z, \lambda_{\text{ex}}) = 2\pi \int_0^\pi P_l(\cos \theta') L^{(0)}(z, \theta', \lambda_{\text{ex}}) \times \sin \theta' d\theta',$$

$$\beta_{\text{in}}(z, \psi, \lambda_{\text{ex}} \rightarrow \lambda) = \frac{1}{4\pi} \sum_{l=0}^N b_{\text{in}}^{(l)}(z, \lambda_{\text{ex}} \rightarrow \lambda) P_l(\cos \psi). \quad (\text{A1})$$

In these equations,  $P_l$  is the Legendre polynomial of order  $l$ ,  $N = 0$  for isotropically emitted fluorescence, and  $N = 2$  for Raman scattering. The total inelastic-scattering coefficient  $b_{\text{in}}^{(0)}$  is

$$\begin{aligned} b_{\text{in}}^{(0)}(z, \lambda_{\text{ex}} \rightarrow \lambda) &\equiv b_{\text{in}}(z, \lambda_{\text{ex}} \rightarrow \lambda) \\ &= \int_{\Xi'} \beta_{\text{in}}(z; \theta', \phi' \rightarrow \theta, \phi; \lambda_{\text{ex}} \rightarrow \lambda) d\Omega' \\ &= 2\pi \int_0^\pi \beta_{\text{in}}(z, \psi, \lambda_{\text{ex}} \rightarrow \lambda) \sin \psi d\psi. \end{aligned}$$

$E_l$  for  $l = 0$  is just the scalar irradiance at  $\lambda_{\text{ex}}$ , whereas  $E_l$  for  $l = 1$  is the net irradiance  $E_d - E_u$  at  $\lambda_{\text{ex}}$ . The inelastic component of the irradiance at  $\lambda$  depends only on the irradiances at the excitation wavelength(s) and on the  $b_{\text{in}}^{(l)}$  coefficients for the particular process.

For Raman scattering,  $\beta_{\text{in}} \equiv \beta_{\text{Ram}}$ , and the angular distribution of  $\beta_{\text{Ram}}$  is given by

$$\beta_{\text{Ram}}(z, \psi, \lambda_{\text{ex}} \rightarrow \lambda) = \tilde{\beta}_{\text{Ram}}(\psi) b_{\text{Ram}}(z, \lambda_{\text{ex}} \rightarrow \lambda), \quad (\text{A2})$$

where  $\tilde{\beta}_{\text{Ram}}(\psi)$  is given by Eq. (9). Substituting Eq. (9) into Eq. (A2) and rewriting in terms of the Le-

gendre polynomials and the quantity  $\gamma \equiv (1 - \rho)/(1 + 3\rho)$  gives

$$\begin{aligned} \beta_{\text{Ram}} &= \frac{3}{16\pi} \left( \frac{1 + 3\rho}{1 + 2\rho} \right) \left[ 1 + \frac{1}{3} \gamma + \frac{2}{3} \gamma P_2(\cos \psi) \right] \\ &\times b_{\text{Ram}}(z, \lambda_{\text{ex}} \rightarrow \lambda). \end{aligned} \quad (\text{A3})$$

Comparing Eqs. (A1) and (A3) reveals that

$$\begin{aligned} b_{\text{Ram}}^{(0)}(z, \lambda_{\text{ex}} \rightarrow \lambda) &= b_{\text{Ram}}(z, \lambda_{\text{ex}} \rightarrow \lambda), \\ b_{\text{Ram}}^{(2)} &= \frac{1}{2} \left( \frac{1 - \rho}{1 + 2\rho} \right) b_{\text{Ram}}(z, \lambda_{\text{ex}} \rightarrow \lambda), \end{aligned}$$

and that all of the other  $b_{\text{Ram}}^{(l)}$  are zero. Finally, the  $\phi$ -averaged source function for Raman scattering is given by

$$\begin{aligned} S_{\text{Ram}}(z, \theta, \lambda) &= \frac{1}{4\pi} \int b_{\text{Ram}}(z, \lambda_{\text{ex}} \rightarrow \lambda) E_0(z, \lambda_{\text{ex}}) \\ &\times \left[ 1 + \frac{1}{2} \left( \frac{1 - \rho}{1 + 2\rho} \right) \frac{E_2(z, \lambda_{\text{ex}})}{E_0(z, \lambda_{\text{ex}})} P_2(\cos \theta) \right] d\lambda_{\text{ex}}. \end{aligned}$$

In general, at the emission wavelength  $\lambda$ , the source function resulting from a narrow band of excitation wavelengths  $\Delta\lambda_{\text{ex}}$  is

$$\begin{aligned} S_{\text{in}}(z, \theta, \lambda) &= \frac{1}{4\pi} b_{\text{in}}(z, \lambda_{\text{ex}} \rightarrow \lambda) \Delta\lambda_{\text{ex}} E_0(z, \lambda_{\text{ex}}) \\ &\times \sum_{l=0}^N \frac{b_{\text{in}}^{(l)}(z, \lambda_{\text{ex}} \rightarrow \lambda) E_l(z, \lambda_{\text{ex}})}{b_{\text{in}}(z, \lambda_{\text{ex}} \rightarrow \lambda) E_0(z, \lambda_{\text{ex}})} P_l(\cos \theta). \end{aligned} \quad (\text{A4})$$

To simulate the irradiances at  $\lambda$ , the basic Monte Carlo code for elastic scattering only is run at  $\lambda_{\text{ex}}$  to determine  $E_l(z, \lambda_{\text{ex}})$ . Then Eq. (A4) is used to inject inelastically scattered photons into the medium with the proper distribution in  $z$  and  $\theta$ . One way to do this is to choose  $z$  from the probability density  $p(z)$  given by

$$p(z) = \frac{E_0(z, \lambda_{\text{ex}})}{\int_0^\infty E_0(z, \lambda_{\text{ex}}) dz}.$$

Thus, given a random number  $\rho_j$  from the sequence  $\dots \rho_j, \rho_{j+1}, \rho_{j+2}, \dots$ ,  $z$  is found from

$$\rho_j = \int_0^z p(z') dz'.$$

Given  $z$ , we then choose  $\theta$  from the conditional density  $p(\theta|z)$  given by

$$p(\theta|z) = \frac{1}{4\pi} \sum_{l=0}^N \frac{b_{\text{in}}^{(l)}(z, \lambda_{\text{ex}} \rightarrow \lambda) E_l(z, \lambda_{\text{ex}})}{b_{\text{in}}(z, \lambda_{\text{ex}} \rightarrow \lambda) E_0(z, \lambda_{\text{ex}})} P_l(\cos \theta),$$

so that

$$\rho_{j+1} = \int_0^{\theta} p(\theta'|z) d\theta'.$$

Finally, the rest of the source function must be incorporated into a photon weight

$$W = b_{\text{in}}(z, \lambda_{\text{ex}} \rightarrow \lambda) \Delta \lambda_{\text{ex}} \int_0^{\infty} E_0(z, \lambda_{\text{ex}}) dz,$$

so that  $S_{\text{in}}(z, \theta, \lambda) = Wp(z)p(\theta|z)$  as required. Once a photon is emitted at  $\lambda$ , it is followed in a manner similar to that which would be used in the absence of inelastic scattering, with the exception that inelastic scattering from  $\lambda$  to longer wavelengths is included by increasing the absorption coefficient  $a(z, \lambda)$  by the appropriate inelastic-scattering coefficient  $b_{\text{in}}(z, \lambda \rightarrow \lambda')$  with  $\lambda < \lambda'$  (recall, however, the discussion of this point in the definition of problem 7). In the code,  $E_0(z, \lambda_{\text{ex}})$  is normalized to unit irradiance at  $\lambda_{\text{ex}}$  entering the top of the atmosphere normal to the solar beam, so the computed irradiances at  $\lambda$  (as seen in Table 6) are for unit irradiance at  $\lambda_{\text{ex}}$  entering the top of the atmosphere. This simulation technique was in part developed in this manner so that it could be used with experimental measurements of  $E_i$  to predict the inelastically scattered irradiances for a given process, e.g., Raman scattering. Such measurements can be obtained using instrumentation developed by Voss.<sup>61,62</sup>

C. D. Mobley began this study with support from the Science Officer Research Program while he was at the Office of Naval Research (ONR); subsequent work was performed while he was a National Research Council Research Associate at the Jet Propulsion Laboratory. H. R. Gordon acknowledges support for this work from the Oceanic Optics Program of the ONR under grant N00014-89-J-1985. G. W. Kattawar was supported in part by the Oceanic Optics Program of the ONR under grant N00014-89-J-1467. A. Morel is grateful for support from the Centre National de la Recherche Scientifique and from the European Space Agency under grant OT/MM/612. P. Reinertman performed this work while supported by National Aeronautics and Space Administration grants NAGW-465 and NAS5-30779, and by ONR grant N00014-89-J-1091. K. Stamnes acknowledges support by the National Science Foundation through grant DPP92-00747 and by the Department of Energy through contract 091574-A-Q1. R. H. Stavn acknowledges the stimulation, support, and constructive criticism of Alan Weidemann and Rudolph Hollman of the Naval Research Laboratory, Stennis Space Center, Miss. Grants of time on the Cray Y-MP were given by the North Carolina Supercomputing Center and the Primary Oceanographic Prediction System, U.S. Naval Oceanographic Office.

R. H. Stavn is grateful for continuing support from the Oceanic Optics Program, ONR, under grant N00014-89-J-3137.

## References

1. F. Kneizys, E. Shettle, L. Abreu, J. Chetwynd, G. Anderson, W. Gallery, J. Selby, and S. Clough, "Users guide to LOWTRAN-7," Rep. AFGL-TR-88-0177 (U.S. Air Force Geophysics Laboratory, Hanscom Air Force Base, Mass., 1988).
2. C. Mobley, "A numerical model for the computation of radiance distributions in natural waters with wind-roughened surfaces," *Limnol. Oceanogr.* **34**, 1473-1483 (1989).
3. C. Mobley and R. Preisendorfer, "A numerical model for the computation of radiance distributions in natural waters with wind-roughened surfaces," NOAA Tech. Memo. ERL PMEL-75 (NTIS PB88-192703) (Pacific Marine Environmental Laboratory, Seattle, Wash., 1988).
4. R. Preisendorfer and C. Mobley, "Albedos and glitter patterns of a wind-roughened sea surface," *J. Phys. Oceanogr.* **16**, 1293-1316 (1986).
5. A. Harrison and C. Coombes, "Angular distribution of clear sky short wavelength radiance," *Sol. Energy* **40**, 57-69 (1988).
6. R. Preisendorfer, "Eigenmatrix representations of radiance distributions in layered natural waters with wind-roughened surfaces," NOAA Tech. Memo. ERL PMEL-76 (NTIS PB88-188701) (Pacific Marine Environmental Laboratory, Seattle, Wash., 1988).
7. C. Mobley, "A numerical model for the computation of radiance distributions in natural waters with wind-roughened surfaces, part II: users' guide and code listing," NOAA Tech. Memo. ERL PMEL-81 (NTIS PB88-246871) (Pacific Marine Environmental Laboratory, Seattle, Wash., 1988).
8. Z. Jin and K. Stamnes, "Radiative transfer in nonuniformly refracting layered media such as the atmosphere-ocean system," *Appl. Opt.* (to be published).
9. K. Stamnes and R. A. Swanson, "A new look at the discrete ordinate method for radiative transfer calculations in anisotropically scattering atmospheres," *J. Atmos. Sci.* **38**, 387-399 (1981).
10. K. Stamnes and H. Dale, "A new look at the discrete ordinate method for radiative transfer calculations in anisotropically scattering atmospheres. II: Intensity computations," *J. Atmos. Sci.* **38**, 2696-2706 (1981).
11. K. Stamnes, S. C. Tsay, W. Wiscombe, and K. Jayaweera, "Numerically stable algorithm for discrete-ordinate-method radiative transfer in multiple scattering and emitting layered media," *Appl. Opt.* **27**, 2502-2509 (1988).
12. H. Gordon, O. Brown, and M. Jacobs, "Computed relationships between the inherent and apparent optical properties of a flat homogeneous ocean," *Appl. Opt.* **14**, 417-427 (1975).
13. H. Gordon, "A bio-optical model describing the distribution of irradiance at the sea surface resulting from a point source embedded in the ocean," *Appl. Opt.* **26**, 4133-4148 (1987).
14. H. Gordon, "Can the Lambert-Beer law be applied to the diffuse attenuation coefficient of ocean water?" *Limnol. Oceanogr.* **34**, 1389-1409 (1989).
15. H. Gordon, "Dependence of the diffuse reflectance of natural waters on the sun angle," *Limnol. Oceanogr.* **34**, 1484-1489 (1989).
16. H. Gordon, "Diffuse reflectance of the ocean: influence of nonuniform phytoplankton pigment profile," *Appl. Opt.* **31**, 2116-2129 (1992).
17. Y. Ge, H. Gordon, and K. Voss, "Simulation of inelastic-scattering contributions to the irradiance field in the oceanic variation in Fraunhofer line depths," *Appl. Opt.* **32**, 4028-4036 (1993).

18. C. Cox and M. Munk, "Statistics of the sea surface derived from sun glitter," *J. Mar. Res.* **13**, 198–227 (1954).
19. L. Elterman, "UV, visible, and IR attenuation for altitudes to 50 km," Rep. AFCRL-68-0153 (U.S. Air Force Cambridge Research Laboratory, Bedford, Mass., 1968).
20. G. Mie, "Beiträge zur Optik trüber Medien, speziell Kolloidalen Metall-Lösungen," *Ann. Phys.* **25**, 377–445 (1908).
21. D. Deirmendjian, "Scattering and polarization properties of polydisperse suspensions with partial absorption," in *Electromagnetic Scattering*, M. Kerker, ed. (Pergamon, New York, 1963), pp. 171–189.
22. G. Kattawar and X. Xu, "Filling-in of Fraunhofer lines in the ocean by Raman scattering," *Appl. Opt.* **31**, 1055–1065 (1992).
23. G. Kattawar and C. Adams, "Stokes vector calculations of the submarine light field in an atmosphere-ocean with scattering according to a Rayleigh phase matrix: effect of interface refractive index on radiance and polarization," *Limnol. Oceanogr.* **34**, 1453–1472 (1989).
24. G. Kattawar and C. Adams, "Errors in radiance calculations induced by using scalar rather than Stokes vector theory in a realistic atmosphere-ocean system," in *Ocean Optics X*, R. W. Spinrad, ed., *Proc. Soc. Photo-Opt. Instrum. Eng.* **1302**, 2–12 (1990).
25. C. Adams and G. Kattawar, "Effect of volume scattering function on the errors induced when polarization is neglected in radiance calculations in an atmosphere-ocean system," *Appl. Opt.* **20**, 4610–4617 (1993).
26. G. Kattawar and C. Adams, "Errors induced when polarization is neglected in radiance calculations for an atmosphere-ocean system," in *Optics of the Air-Sea Interface: Theory and Measurement*, L. Estep, ed., *Proc. Soc. Photo-Opt. Instrum. Eng.* **1749**, 2–22 (1992).
27. G. Plass and G. Kattawar, "Radiative transfer in an atmosphere-ocean system," *Appl. Opt.* **8**, 455–466 (1969).
28. G. Plass and G. Kattawar, "Monte-Carlo calculations of radiative transfer in the earth's atmosphere ocean system: I. Flux in the atmosphere and ocean," *J. Phys. Oceanogr.* **2**, 139–145 (1972).
29. H. Gordon and O. Brown, "Irradiance reflectivity of a flat ocean as a function of its optical properties," *Appl. Opt.* **12**, 1549–1551 (1973).
30. G. Plass, G. Kattawar, and J. Guinn, Jr., "Radiative transfer in the earth's atmosphere and ocean: influence of ocean waves," *Appl. Opt.* **14**, 1924–1936 (1975).
31. A. Morel and B. Gentili, "Diffuse reflectance of oceanic waters: its dependence on sun angle as influenced by the molecular scattering contribution," *Appl. Opt.* **30**, 4427–4438 (1991).
32. A. Morel and B. Gentili, "Diffuse reflectance of oceanic waters. II. bidirectional aspects," *Appl. Opt.* (to be published).
33. D. Tanré, M. Herman, R. Deschamps, and A. deLefre, "Atmospheric modeling for space measurements of ground reflectances including bi-directional properties," *Appl. Opt.* **18**, 3587–3594 (1979).
34. K. Baker and R. Frouin, "Relation between photosynthetically available radiation and total insolation at the ocean surface under clear skies," *Limnol. Oceanogr.* **32**, 1370–1377 (1987).
35. J. Kirk, "Monte Carlo procedure for simulating the penetration of light into natural waters," Div. Plant Industry Tech. Paper 36 (Commonwealth Scientific and Industrial Research Organization, Canberra, Australia, 1981).
36. H. Gordon and D. Castano, "Coastal zone color scanner atmospheric correction algorithm: multiple scattering effects," *Appl. Opt.* **26**, 2111 (1987).
37. W. Blatter, H. Horak, D. Collins, and M. Wells, "Monte Carlo studies of the sky radiation at twilight," *Appl. Opt.* **13**, 534 (1974).
38. R. Stavn and A. Weidemann, "Optical modeling of clear oceanlight fields: Raman scattering effects," *Appl. Opt.* **27**, 4002–4011 (1988).
39. R. Stavn and A. Weidemann, "Raman scattering in ocean optics: quantitative assessment of internal radiant emission," *Appl. Opt.* **31**, 1294–1303 (1992).
40. D. Brine and M. Iqbal, "Diffuse and global solar spectral irradiance under cloudless skies," *Sol. Energy* **30**, 447–453 (1983).
41. T. Petzold, "Volume scattering functions for selected ocean waters," SIO Ref. 72–78 (Scripps Institution of Oceanography, La Jolla, Calif., 1972).
42. A. Morel, "Optical properties of pure water and pure sea water," in *Optical Aspects of Oceanography*, N. G. Jerlov and E. S. Nielsen, eds. (Academic, New York, 1974), pp. 1–24.
43. R. Smith and K. Baker, "Optical properties of the clearest natural waters (200–800 nm)," *Appl. Opt.* **20**, 177–184 (1981).
44. L. Prieur and S. Sathyendranath, "An optical classification of coastal and oceanic water based on the specific spectral absorption curves of phytoplankton pigments, dissolved organic matter, and other particulate materials," *Limnol. Oceanogr.* **26**, 671–689 (1981).
45. H. Gordon and A. Morel, "Remote assessment of ocean color for interpretation of satellite visible imagers, a review," in *Lecture Notes on Coastal and Estuarine Studies* (Springer Verlag, Berlin, 1983), Vol. 4.
46. M. Lewis, J. Cullen, and T. Platt, "Phytoplankton and thermal structure in the upper ocean: consequences of nonuniformity in chlorophyll profile," *J. Geophys. Res.* **88**, 2565–2570 (1983).
47. T. Platt and S. Sathyendranath, "Oceanic primary production: estimation by remote sensing at local and regional scales," *Science* **241**, 1613–1620 (1988).
48. S. Porto, "Angular dependence and depolarization ratio of the Raman effect," *J. Opt. Soc. Am.* **56**, 1585–1589 (1966).
49. R. Preisendorfer, *Properties*, Vol. V of *Hydrologic Optics* (U.S. Department of Commerce, Pacific Marine Environmental Laboratory, Seattle, Wash., 1976).
50. G. Kattawar and G. Plass, "Asymptotic radiance and polarization in optically thick media: ocean and clouds," *Appl. Opt.* **15**, 3166–3178 (1976).
51. R. Stavn, R. Schiebe, and C. Gallegos, "Optical controls on the radiant energy dynamics of the air/water interface: the average cosine and the absorption coefficient," in *Ocean Optics VII*, M. A. Blizard, ed., *Proc. Soc. Photo-Opt. Instrum. Eng.* **489**, 62–67 (1984).
52. G. Plass, T. Humphreys, and G. Kattawar, "Ocean-atmosphere interface: its influence on radiation," *Appl. Opt.* **20**, 917–931 (1981).
53. H. van de Hulst, *Multiple Light Scattering: Tables, Formulas, and Applications* (Academic, New York, 1980), Vol. 1.
54. L. Prieur and A. Morel, "Etude theorique du regime asymptotique: relations entre caracteristiques optiques et coefficient d'extinction relatif a la penetration de la lumiere du jour," *Cah. Oceanogr.* **23**, 35 (1971).
55. J. Mueller and R. Austin "Ocean optics protocols for SeaWiFS validation," SeaWiFS Project Tech. Rep. Vol. 5, S. B. Hooker and E. R. Firestone, series eds., NASA Tech. Memo. 104566 (National Aeronautics and Space Administration, Washington, D.C., July 1992).
56. H. Gordon, "Ship perturbation of irradiance measurements at sea. I: Monte Carlo simulations," *Appl. Opt.* **24**, 4172–4182 (1985).
57. C. Adams and G. Kattawar, "Radiative transfer in spherical shell atmospheres: Rayleigh scattering," *Icarus* **35**, 139–151 (1978).
58. G. Kattawar and C. Adams, "Radiative transfer in spherical shell atmospheres. II. asymmetric phase functions," *Icarus* **35**, 436–449 (1978).

59. G. Kattawar, "Radiative transfer in spherical shell atmospheres. III. application to Venus," *Icarus* **40**, 60-66 (1979).
60. S. Chandrasekhar, *Radiative Transfer* (Dover, New York, 1960).
61. K. Voss, "Electro-optic camera system for measurement of the underwater radiance distribution," *Opt. Eng.* **28**, 241-247 (1989).
62. K. Voss, "Use of the radiance distribution to measure the optical absorption coefficient in the ocean," *Limnol. Oceanogr.* **34**, 1614-1622 (1989).